TEMPERATURE DEPENDENCE OF ZERO PHONON LINE EMISSION FROM DEFECTS IN HEXAGONAL BORON NITRIDE AND DESIGN OF PHOTON-PAIR SOURCE

A Thesis Submitted to
the Graduate School of Engineering and Sciences of
İzmir Institute of Technology
in Partial Fulfillment of the Requirements for the Degree of

MASTER OF SCIENCE

in Physics

by
Nahit Polat

September 2017
İZMİR

We approve the thesis of **Nahit Polat**

Assoc. Prof. Dr. Serkan ATEŞ
Department of Physics, İzmir Institute of Technology

Assoc. Prof. Dr. Özgür ÇAKIR
Department of Physics, İzmir Institute of Technology

Assoc. Prof. Dr. Mehmet Ertuğrul SOLMAZ
Department of Electrical and Electronics Engineering, İzmir Katip Celebi University

21 September 2017

Prof. Dr. Tuğrul SENGER
Head of the Department of
Department of Physics

Prof. Dr. Aysun SOFUOĞLU
Dean of the Graduate School of
Engineering and Sciences

ACKNOWLEDGMENTS

I would like to thank all of those people who helped me through this thesis work. I would like to thank my advisor, Assoc. Prof Serkan ATEŞ for his support and understanding.

I would like to thank Assoc. Prof. Dr. Yusuf SELAMET and Ozan ARI for his material and laboratory support.

I also thank my thesis committee: Assoc. Prof. Özgür ÇAKIR and Assoc. Prof. Dr. Mehmet Ertuğrul SOLMAZ.

Thanks to my group friends: Volkan FIRAT, Elif Özçeri, Yağız OYUN and Mehmet ÖZCAN for supports and helps.

ABSTRACT

TEMPERATURE DEPENDENCE OF ZERO PHONON LINE EMISSION FROM DEFECTS IN HEXAGONAL BORON NITRIDE AND DESIGN OF PHOTON-PAIR SOURCE

This thesis presents studies of the defect centers in hBN and design of nonlinear waveguide. The multilayer hBN flakes and Si_3N_4 waveguide are available materials in modern nanophotonics applications.

The color centers in hBN are consisted of quantized states because each defect center has different saturation power and dipole polarization. The line shape of emission from defect centers is directly depended photon vibrations and temperature of sample. Moreover, phonon bands in the color centers affect the wavelength of emission and we statistically worked on the phonon effects on ZPL.

The Si_3N_4 waveguide can be more efficient chip scale photon pair sources to create entangled photons in visible band. The zero dispersion wavelength calculations give an efficient waveguide geometry as 650×600 nm^2 for 780 nm pump wavelength.

ÖZET

ALTIGEN BOR NİTRÜRDEKİ KUSUR MERKEZLERİNDEN SICAKLIĞA BAĞLI SIFIR FONON ÇİZGİSİ IŞIMASI VE FOTON-ÇİFTİ KAYNAĞI TASARIMI

Bu tez altıgen bor nitrürdeki kusur merkezleri üzerine yapılan çalışmaları ve lineer olmayan dalga kılavuzu tasarınımını gösterir. Çok katmanlı hBN pulları ve silikon nitrür modern nanofotonik uygulamaları için uygun malzemelerdir.

hBN'deki renk merkezleri kesikli enerji seviyelerinden oluşur, çünkü her bir kusur merkezi farklı doyum güçlerine ve dipol kutuplaşmalarına sahiptir. Kusur merkezlerinden gelen ışımanın çizgi şekli doğrudan phonon titreşimleri ve örneğin sıcaklığı ile ilgilidir. Ayrıca, renk merkezlerindeki fonon bantları ışımanın dalga boyunu etkiler ve istatistiksel fononların sıfır fonon çizgisine etkisini çalıştık.

Dolanık foton çifti üretmek için Si_3N_4 dalga kılavuzu görünür bölgede çok verimli çip ölçekli foton çifti kaynağı olabilir. Sıfır dağılım dalga boyu hesaplamaları 780 nm pompa dalga boyu için verimli bir dalga kılavuzu geometrisini 650×600 nm^2 olarak verir.

TABLE OF CONTENTS

LIST OF FIGURES

Figure **Page**

CHAPTER 1

INTRODUCTION

In the past several decades, many critical steps in building a quantum computer are achieved with quantum information. The building a qubit is the main part of quantum information (Steane, 1998). Single atoms and single photons are available sources in quantum computing (Monroe, 2002) and also photon-pairs can be used for qubits (Silverstone et al., 2015). Quantum dots (Michler, 2000) and nitrogen vacancy centers in diamond (Kurtsiefer et al., 2000) are common semiconductor single photon sources in the literature. After two dimensional material revolution (The Nobel Prize in Physics 2010), new materials which are transition metal dichalcogenides (Srivastava et al., 2014) and defect centers in hexagonal boron nitride flakes (Tran et al., 2016), may be decided a new route for single photon sources because scalability of two dimensional materials is more available for chip technology. Additionally, the defect centers in diamond with paramagnetic impurities are the functional sources for quantum computing (Gordon et al., 2013). The control of magnetic states in two dimensional materials is used to build qubit states (Huang et al., 2012) and different vacancies with carbon, nitrogen, oxygen etc., in hexagonal boron nitride (Tawfik et al., 2017) can be a sufficient source for quantum computing. The color centers in monolayer hexagonal boron nitride can be useful for building qubits, due to robust, scalable and quantum emission at room temperature.

The single photon sources have a key part of application in quantum technologies. Moreover, the other popular method for quantum technologies is creating the entangled photon-pairs. The most important condition in this method is entanglement. The quantum entanglement means that photon-pairs are linked together in a way and lose their identity. Additionally, when one particle's quantum state is measured, the possible quantum states of the other particles can be determined. The available applications in quantum technologies can be make with the uncertainty in quantum states of the particles and determination of quantum state of unmeasured particles. The most important applications with entangled photon-pairs are the information and communications technology applications (Thylén and Wosinski, 2014), quantum sensing and metrology (Dowling et al., 2015). Additionally, the nonlinear crystals can be used to create entangled photon-pairs. The crystals have different type of susceptibilities, second order susceptibility ($\chi^{(2)}$) and third order susceptibility ($\chi^{(3)}$). If nonlinear crystal has second order susceptibility, three

waves (signal, idler and pump waves) are mixed and, signal and idler waves are entangled photons. This method is known as spontaneous parametric down conversion (SPDC) process. If nonlinear crystal has third order susceptibility, four waves (signal, idler and two pump waves) are mixed and, signal and idler waves are entangled photons. This method is known as spontaneous four wave mixing (SFWM) process. In contemporary times, complementary metal oxide semiconductor (CMOS)technology is more popular for photon pair generation. CMOS technology is used in integrated circuit for computers. Therefore, integrated waveguides can be an useful method for new generation computer and quantum computation. As a result, we design a Si_3N_4 waveguide for photon pair generation.

In this thesis, we will discuss that temperature how to affect the optical emission from defects center in hBN flakes, and second part of thesis we will design a Si_3N_4 waveguide work on visible band with SFWM process. The hBN defect centers are a single photon source and the waveguide is a photon-pair source.

CHAPTER 2

TEMPERATURE DEPENDENCE OF ZERO PHONON LINE EMISSION FROM DEFECTS IN HEXAGONAL BORON NITRIDE

Boron nitride has sp^2 hybridization between boron ($1s^2$, $2s^2$, 2p) and nitrogen ($1s^2$, $2s^2$, $2p^3$) and known as 'white graphene'. It is an important material for the industry because it has a wide band gap and unique electronic structure properties about thermal and electronic stability.

In the first instance, theoretical calculations about hBN energy levels was begun with R. Taylor and C. A. Coulson in 1952 (Taylor and Coulson, 1952) and Simon Larach and Ross E. Shrader worked on optical properties with luminescence measurements in 1956 (Larach and Shrader, 1956). E. Doni and G. Pastori Paravicini studied on optical properties of hBN theoretically and experimentally in 1969 (Doni and Parravicini, 1969). The scientists accepted that hBN is an insulator with a direct band gap of $\sim$6 eV, so the research on hBN concentrated upon thermal and electronic properties of hBN. Discovery of graphene might represents a more accessible route toward investigate the optical properties of mono and multi layer hBN that is two dimensional (2D) material. In addition, the few layer hBN is a semiconductor that has an indirect bandgap at 5.955 eV (Cassabois et al., 2016). Otherwise, the new energy levels might be occured in 2D hBN as a result of point defect centers that have irregular atomic structure or missing an atom in the lattice. The first optical characterization of hBN layers in the literature has been shown with single photon emission (Tran et al., 2016).

In this thesis, defects center in hBN has been chosen, because it is a single photon source at low temperature (at 4 K) (Jungwirth et al., 2016), high temperature (800 K) (Kianinia et al., 2017) and also room temperature. Moreover, it is robust and scalable material for chip technology.

This chapter of thesis is about the optical properties of defect centers on hexagonal boron nitride (hBN). Firstly, we will explain why we use hBN and our experimental set-up. Secondly, we will clarify the ZPL emission from quantized state on hBN defect centers with saturation power and dipole properties of color centers. Thirdly, we will discuss phonon vibration how to effect line shape of ZPL emissions and how to be efeected

from temperature. Finally, we will represent our statistical results of ZPL emission from hBN defect centers.

2.1. Experimental Setup

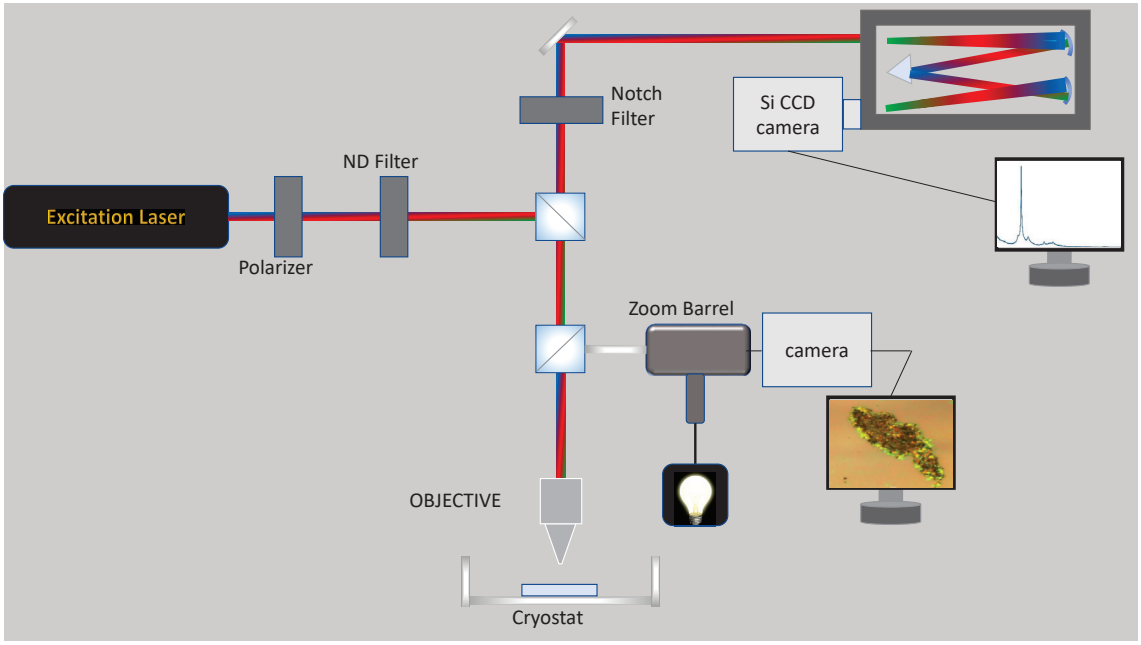

Figure 2.1. Schematic illustration of the μPL set-up

The boron nitride (BN) flakes solution that comprised of ethanol and water, has been bought from Graphene Supermarket$^{\mathrm{TM}}$. The solution is used to fabricate multilayer hBN flakes. In the sample preparation, 10μL BN flakes solution was dropcasted onto silicon substrate and dried under the room conditions.

Fig 2.1 schematically shows the micro Photo Luminescence (μPL) set-up. In this work, four excitation lasers (continuous wave) that have different wavelengths (488 nm, 514 nm, 532 nm, 633 nm) and polarizers and notch filters for each lasers (specific wavelengths) was utilized for PL and Raman measurements. The excitation lasers are focused onto the sample with two different objectives. First one is Olympus MPLN100x$^{\mathrm{TM}}$ that has a high numerical aperture (N.A. = 0.9) and focal length of objective is 0.21 mm. It is only used in room temperature measurements. Second one is Olympus LMPLFLN50x$^{\mathrm{TM}}$ that has 0.5 numerical aperture and objective focal length is 10.6 mm. It is used in cryogenic temperature measurements because of high focal length. The set-up has motorize

x-y stage and z axis at the objective part for mapping the sample. In cryogenic measurements, Linkam THMS600$^{\mathbf{TM}}$ is used to cool the sample with liquid nitrogen to -196^{o}C ($\sim$78K). The distance between sample holder in the cryostat and upper lid window is 3.5 mm, thus we could not use 100x objective in low temperature measurements. The μPL set-up describes different sensitivity in PL and Raman spectrum through a 75 cm focal length Princiton Instruments$^{\mathbf{TM}}$ monochromator with selectable slit sizes and gratings (150 grooves(gr)/mm, 600 (gr)/mm, 1800 (gr)/mm). The monochromator focused the light onto CCD camera (ProEM-EMCCDs Detector$^{\mathbf{TM}}$, 1600x200 pixels) that is cooled to -75^{o}C (with CoolCube recirculator) and has $\sim$80$\%$ quantum efficiency at 500 to 700 nm and also the maximum resolution of the detector is 0.0086 nm.

In Raman, photo-luminescence and low temperature measurements, we employed with the μPL set-up during this work.

2.2. Raman and Photo-Luminescence Measurements

In this section we discuss on physical meaning of Raman and photo-luminescence (PL) measurements. Moreover, we could expound theoretical meaning of PL measurements on hBN.

2.2.1. Raman Spectroscopy

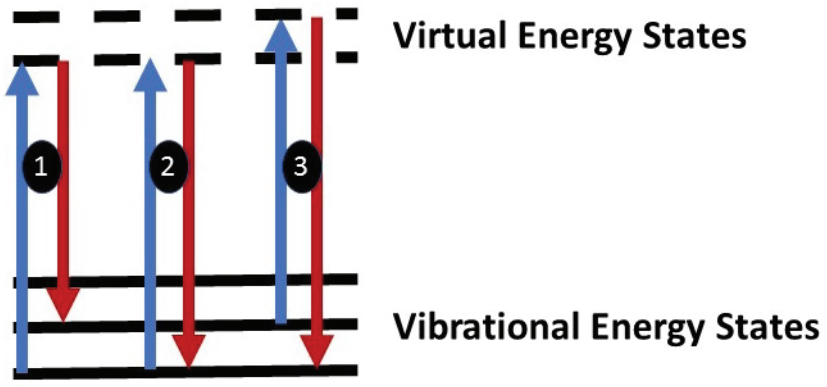

Figure 2.2. A schematic Raman spectrum. First one is Stokes scattering, second one is Rayleigh scattering and last one is Anti-stokes scattering

When a beam of light is focused onto a molecule, it absorbs and scatters the photons respectively. The Rayleigh scatter that is second one in Fig 2.2 illustrates same energy levels for absorption (blue arrow) and emission (red arrow). First one is Stokes line that absorption energy is grater than emission and has lower energy than Rayleigh line. The energy of anti-Stokes line in third one of Fig 2.2 is greater than other lines.

The main point of the Raman spectroscopy is inelastic light scattering that is Stokes and anti-Stokes radiations. The reason of inelastic light scattering is basically internal vibration of molecules. Therefore, the energy of inelastic light emission in molecule represent the energy difference of vibrational levels. The energy gap between the vibrational energy levels (Raman Shift) is an unique properties of molecules.

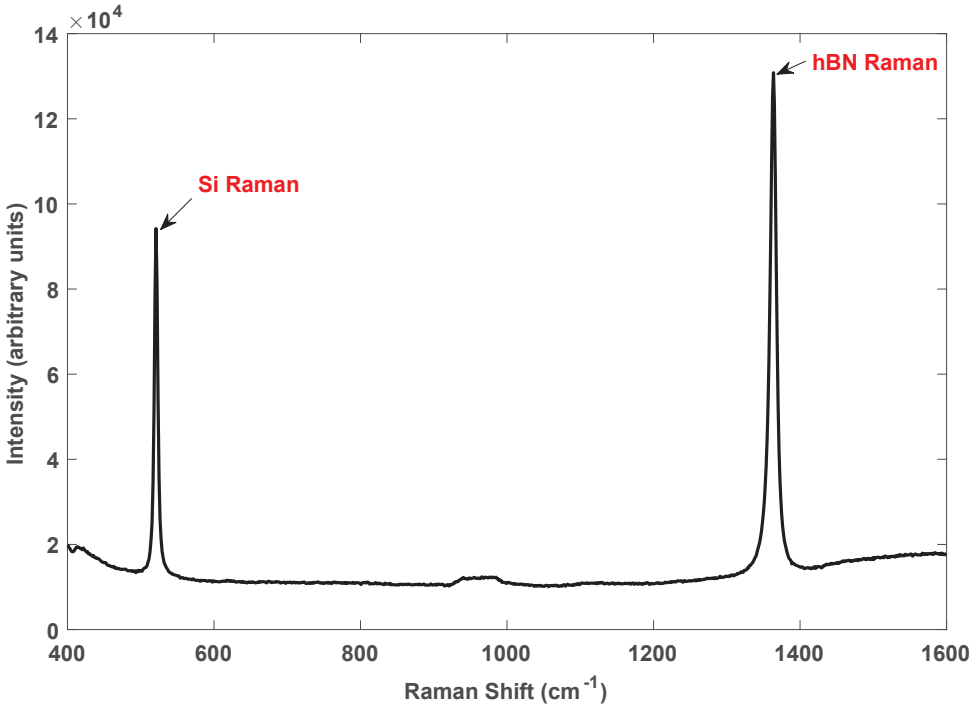

Figure 2.3. Raman spectrum of hBN

The measurement of Raman shift serves to understand the contents of sample with substrate. After the fabrication of sample, we need to check that hBN molecules could be transferred to Si substrate. In Fig 2.3, Raman shift spectrum is shown that hBN comprises some parts of the sample. The left peak is Silicon Raman shift at 520.9 cm^{-1} and the right peak is hBN Raman shift at 1365 cm^{-1} (169 meV) in Fig 2.3. In addition, 169 meV represents the energy difference between vibrational levels.

2.2.2. Photo-Luminescence Properties of hBN

In the next section, we discuss theoretical background of photon emission on defect centers. Moreover, we explain that color centers on hBN are point defect centers, with experimental map results.

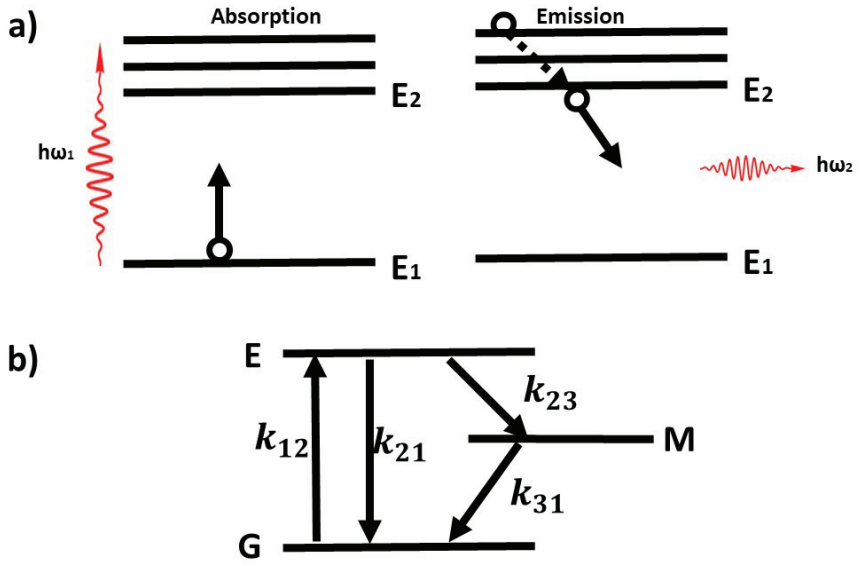

Figure 2.4. a) Schematic illustration of the photon emission, b) Schematic illustration of the photon emission on a color center (G $\rightarrow$ graund state, E $\rightarrow$ exited state, M $\rightarrow$ metastable state)

The molecules are consisted of valance and conduction bands with energy gaps that describe type of molecules as conductor, semiconductor and insulator. The molecules want to be in the stable energy states (because of Pauli exclusion principle that one state has maximum two electrons) so all atoms on minimum energy levels without any external influence. If the photons of energy or the electrical current energy is more than band gap energy ($h\omega_1 > h\omega_2$ in Fig.2.4.a), electrons in valence band is absorbed from available holes in conduction bands, after a relaxation time, electrons are located at minimum conduction energy level and emitted to valance bands with $h\omega_2$ energy (Fig.2.4.a). It is known as luminescence (photo-luminescence is absorbing with a photon of energy electro-luminescence is absorbing with electrical current).

Photo-luminescence (PL) is a basic method to understand the energy levels of the semiconductors. In this thesis, PL spectroscopy is used to work on emission from

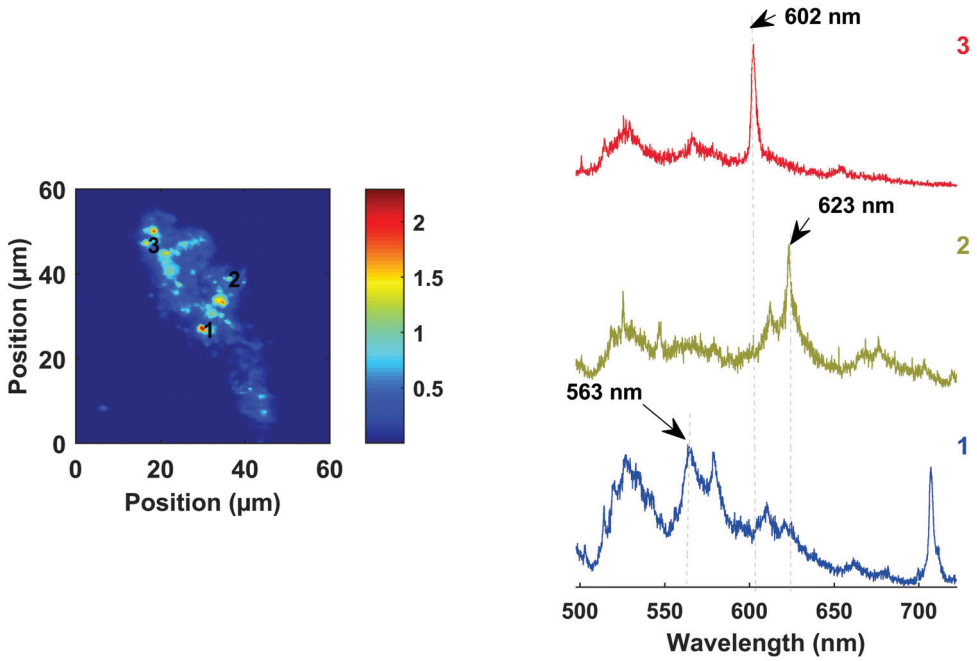

Figure 2.5. A mapping of a multilayer hBN flakes and point defects spectrums with locations

distinguishable point defect centers that have irregular atomic structure or missing an atom in the lattice. The emission from point defects might be described a basic three level system that consist of there different energy states. Fig.2.4.b represents energy levels on color centers, k_{12} is the rate of electron transition ground to excited energy levels, k_{21} is direct emission ratio of main energy levels, k_{23} is the rate of emission from excited state to metastable state that is additional state, is reason of point defect in lattice structure, and k_{32} is the emission ratio of metastable state to ground state.

Figure 2.5 shows three different emission lines from distinguishable point defects. The left part of Fig.2.5 is a map which size is 60μm x 60μm , on a multilayer hBN flakes at room temperature and the location of the selected color centers are seen in left part of the figure. Moreover, the right part of the figure comprises three selected color centers with PL spectrum on hBN. In the map, 488 nm excitation laser, 100x objective (N.A.=0.9) and a motorize x-y stage which step size is 0.2 μm , are used. According to results of the map, the size of defect centers are as small as 0.5 μm. Generally, if the sample has not been applied any defects creation method, irregular structures or missing atoms may only be shown in edge of sample. Therefore, defects are shown on edge of hBN flakes.

2.2.3. Zero Phonon Line

Zero phonon line (ZPL) is a purely electronic transition between the electronic states. The electronic transition with vibrational phonons is known as phonon side band (PSB).

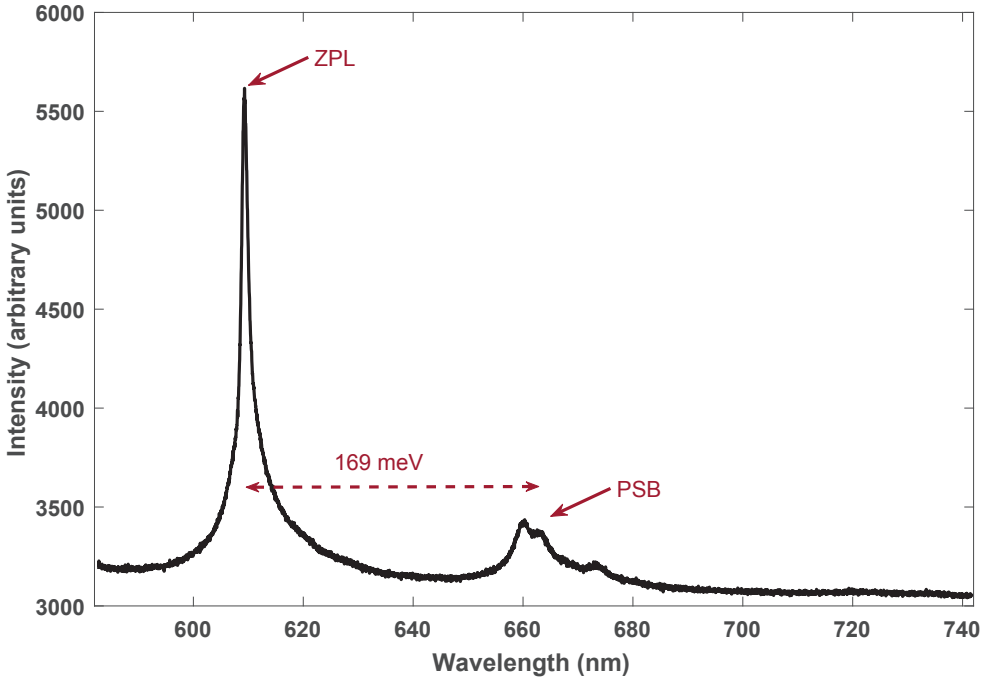

Figure 2.6. A PL spectrum with ZPL and PSB

Figure 2.6 shows a PL spectrum that is excited with 532 nm laser at room temperature with ZPL at 609 nm and PSB at 663 nm. In hBN PL spectrum, energy difference between ZPL and PSB emissions is 169 meV. The energy difference between vibration states was recorded as 169 meV from Raman spectroscopy in section 2.2.1. As a result, reason of PSB emissions is vibration energy levels in electronic ground state. Also, second PSB may be shown in far away ∼340 meV from ZPL.

In this work 500 to 800 nm ZPLs are measured with 488, 514, 532 and 633 nm excited lasers and in the literature (Bourrellier et al. (2016)), ZPL at 4.1 eV (302 nm) was recorded . The measurements show that the defect centers can emit any wavelength (equal or lower than excitation laser energy) with different intensities, if excited laser energy is not more than hBN bandgap . The distribution of emission lines from hBN defect centers will be discussed in 'Statistics' part of the chapter.

2.3. Optical Characterization of the Defects

In this section, the basic optical properties of the color centers on hBN will be discussed with physical background and we will focus on quantized states in point defects. For the reason, power series and polarization series will be contributed to understand that hBN is a single photon emitter.

2.3.1. Excitation Power Series

Figure 2.4.b reveals that the fluorescence intensity (total emission rate) is depended to transition rate between states and life time of defect center (Jelezko and Wrachtrup (2006)). The limit of fluorescence intensity from a color center can be shown as ;

$$I_{max} = \frac{k_{31}(k_{21} + k_{23})\phi_f}{2k_{31} + k_{23}} \tag{2.1}$$

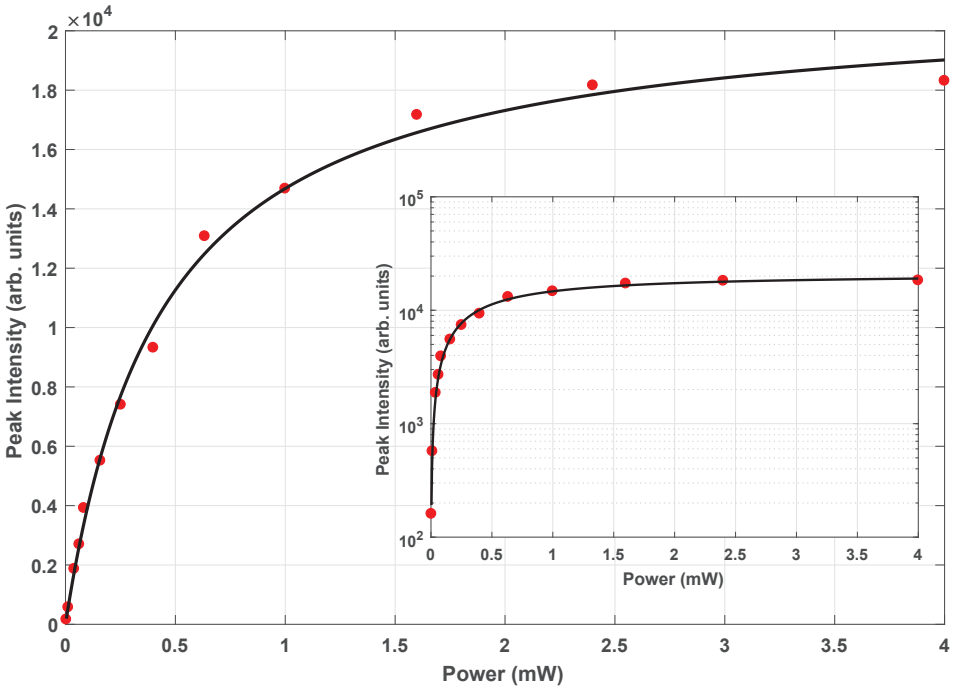

Figure 2.7. Linear and logarithmic saturation curves from a single hBN defect center with $P_{sat} = 0.4363$ mW

where k_{ij} are emission rates and ϕ_f is proportional to the color center lifetime that represents the average time of emission. The absorbed electron number depends the

power of the excitation laser. The number of electron excited from ground state must not be more than the available holes on excited state. Equation 2.1 represents maximum intensity of ZPL emission. The equation is not depend on power of excited laser because the emission from quantized state is directly depended on lifetime of the defect centers. Therefore, more power of excitation laser does not give more brightness emission. I_{max} is the limit of the fluorescence intensity and ZPL emissions on defect centers have a saturation power.

Figure 2.7 represents the power series measurements on an individual defect center as emitted at 563 nm. The motorize neutral density (ND) filter with 488 nm excitation laser on μPL set-up in Fig.2.1 is used to record 13 different powers that are 0.004 mW to 4 mW (The powers are measured after the ND filter on μPL setup). Figure 2.7 describes the limit of fluorescence intensity on a single hBN color center with linear and logarithmic (inside) graph and the results fit with;

$$I = I_{\infty}\frac{P}{P + P_{sat}} \tag{2.2}$$

where I is intensity, I_{∞} is a coefficient, P is power of the excitation after the ND filter and P_{sat} is saturation power of defect center. The saturation power as 0.4363 mW is calculated from Equation 2.2. The logarithmic saturation curve is easily described the saturation power. After $\sim$0.5 mW, we cannot show radical change in peak intensity. Therefore, ZPL is emitted from quantized state in hBN defect centers.

2.3.2. Excitation Polarization Series

The other important measurement to understand the emission from quantized states is the excitation polarization series. If the defect centers have a single transition dipole, the absorption can be demonstrated with sinusoidal behavior;

$$I(\alpha) = I_{min} + I_{\theta}\sin^2(\alpha - \theta) \tag{2.3}$$

where α is the polarization angle of excitation laser, θ is phase shift, $I(\alpha)$ is observed intensity, I_{min} is minimum intensity depend on polarization and I_{θ} is the amplitude of the oscillation. The directions of maximum absorption are given with $\theta\pm$ 90. If we use $\sin(\alpha - \theta \pm 90) = \pm\cos(\alpha - \theta)$ and if the phase shift is equal to zero ($\theta = 0$),

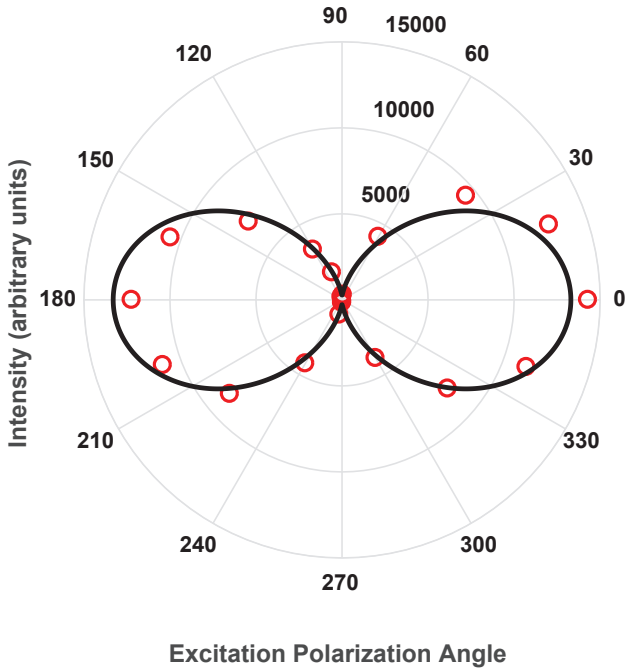

Figure 2.8. Excitation polarization series with 488 nm excitation laser and fluoresence emission in 563 nm

$$I = I_0 \cos^2(\alpha) + I_{min} \tag{2.4}$$

where I_0 is a coefficient.

A specific half wave plate for 488 nm excitation laser is employed to change the polarization of the excitation laser in Fig.2.1 and it is same defect that was employed in power series. The power of laser is chosen near the saturation power ($\sim$0.5mW). The polarization series experiment is consisted of 21 different degree data points in Fig.2.8. The black fitting curve is plotted using the Equation 2.4. The fitting the our data describes the polarization dependence of the hBN defect center and the result is a proof of the emissions from quantized states.

The other important property of emission from the defect centers is visibility that is a control parameter of the absorption in a single transition dipole. It has a basic mathematical approach ;

$$V = \frac{I_{max} - I_{min}}{I_{max} + I_{min}} \tag{2.5}$$

where I_{max} is the maximum and I_{min} is the minimum intensity of the polarization series. The visibility of Fig.2.8 is $\sim 90\%$. Additionally, Exarhos et al. (2017) worked on polarization dependence of hBN emitters with different visibility 20% to 80% and they show that each defects have different degree of ZPL polarization dependence due to optical dipole orientation of each emitters.

2.4. Temperature Dependence Measurements

In the last section, the excitation power and polarization series showed that the reason of emission from hBN defect centers is quantized states. In the section, we will work on the temperature effects on ZPL emission from quantized states in hBN defect centers. Therefore, the interaction between light and phonons in solid will be discussed. Firstly, physical meaning of phonons and electron phonon interaction is the starting point of the section. After the theoretical brief, our experimental results will be clarified with theory.

2.4.1. Phonons

The phonon is a quasiparticle in quantum mechanics. It describes the vibrational motions in a lattice of atoms or molecules. The two sub-division category of phonons are represented with acoustic(A) and optical(O) phonons and they divide two other subcategory: transverse (TA and TO) and longitudinal (LA and LO). The acoustic phonon modes interact directly with light, so acoustic phonons and photons have similar energy and momentum. The optical phonons are shown in relaxation period of photon emission in Fig.2.4.a. In addition, the phonons have Bose-Einstein (BE) statistics;

$$\langle N \rangle = \frac{1}{\exp\left(\left(\epsilon - \mu\right)/k_B T\right) - 1} \tag{2.6}$$

where, $\langle N \rangle$ is the average number of particle, ϵ is the energy of state, μ is chemical potential, k_B Boltzmann constant and T is temperature. The BE statistics show that the probability of phonons on excited states (high energy states) is nearly zero at low temperature. Thus, the effects of phonons to ZPL emission decrease at cryogenic temperature. The temperature dependence of ZPL emission will be diffusively discussed with experimental results.

2.4.2. Electron Phonon Coupling On Defect Centers

In solids, the electronic transition in defect centers from non-degenerate electronic states is affected from vibrations of the surrounding host and change the charge distribution of defects. After the optically excitation of orbitals, they reach a new equilibrium point on charge distribution.

Davies (1981) is used for a road map of theoretical description of electron phonon coupling on defect centers. Mathematical representation begins with a single vibrational mode with an uncoupled system between electronic states and vibration states. The ground state energy of electronic states V_g;

$$V_g = \frac{1}{2} m\omega^2 Q^2 \tag{2.7}$$

where m is effective mass of the mode, ω is angular frequency and Q is the displacement of the nuclei from the equilibrium positions. The excited state energy is similar the ground state energy without energy difference E_e between states;

$$V_e = E_e + \frac{1}{2} m\omega^2 Q^2 \tag{2.8}$$

the Equation 2.8 works with vibration at equilibrium point $Q = 0$.

When the electron-phonon coupling is added to the mathematical representation;

$$V_e = E_e + \frac{1}{2} m\omega^2 Q^2 + aQ + bQ^2 \tag{2.9}$$

where aQ symbolizes the linear electron-phonon coupling and bQ^2 denotes the quadratic electron-phonon coupling. In linear coupling the system does not study the same equilibrium point and the vibration modes work a new equilibrium point.

$$Q_{new} = -\frac{a}{m\omega^2} \tag{2.10}$$

it creates the position shifts in vibrational parabolas between excited and ground states.

After the position shifts, the excited state energy of electronic states are rewritten from Equation 2.9;

$$V_e = E_e + (\frac{1}{2} m\omega^2 + b) \left(Q + \frac{a}{m\omega^2 + 2b} \right)^2 - \frac{a^2}{2m\omega^2 + 4b} \tag{2.11}$$

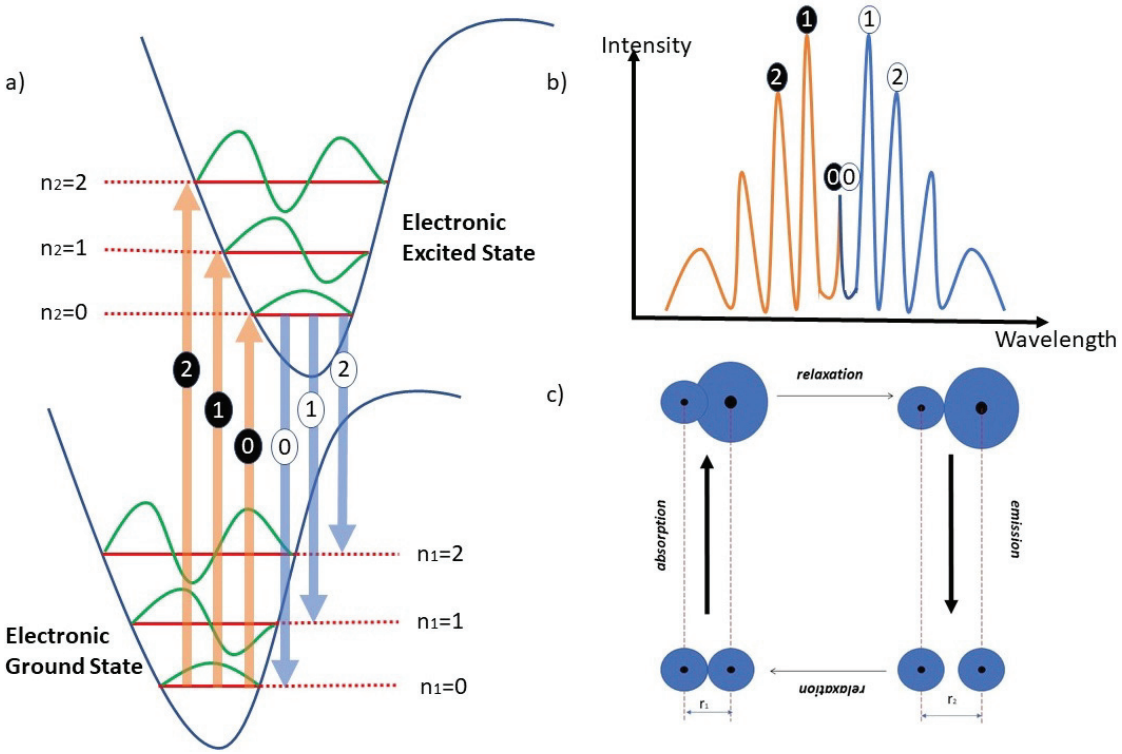

Figure 2.9. a) Configuration diagram of vibrational-electronic transition for two electronic state in a molecule. The orange vertical arrows show allowed absorption lines electronic ground state to excited state and blue arrows is a shematic representation of allowed emission line. b) Schematic representation of probable spectrum of the diagram. c) Shortly description of changes on the radius of nuclei during the absorption and emission of photons (Fox, 2001).

In Equation 2.11, $\frac{1}{2}m\omega^2 + b$ describes the square of frequency, $\Omega = \left(\omega^2 + \frac{2b}{m}\right)^{1/2}$. The calculation about the electron-phonon interaction covers only a single vibrational mode until the Eq.2.11. The general form of electron-phonon coupling is written as ;

$$V_e = E_e + \frac{1}{2}\sum_{i=1}^{n} m_i\omega_i Q_i^2 + \sum_{i=1}^{n} a_i Q_i + \sum_{i=1,j=1}^{n} b_{ij} Q_i Q_j \tag{2.12}$$

The second part of the Equation 2.12 describes the summation of energy of the electronic states, third part is summation of energy of vibrational states and last part is interaction energy.

2.4.3. The Franck-Condon Principle

The Franck Condon principle is a description of electronic transitions in nuclear configuration. Figure 2.9.a shows the absorption and emission energies in the Franck Condon principle. The orange arrows describe possible absorption lines and the blue vertical arrows represent allowed emission lines. The number of arrows have a probability depended on phonon density of state (DOS) of molecule. The phonon DOS of the hBN and defect centers of hBN will be discussed on statistics section.

Figure 2.9.b shows the allowed absorption and emission lines on a defect center. If the excitation energy is equal to the orange zero line and emission energy is equal to blue zero line on Fig.2.9.a and Fig.2.9.b, that is the most possible transition on the Franck Condon diagram.

Figure 2.9.c shows the basic absorption and emission process according to Franck Condon principle. In the first step, the molecules are in the ground state and shown in the lower left corner of Fig.2.9.c and the distance between two nuclei is r_1. When one of the molecule absorbs the photon from excitation laser, an electron is excited and size of the nuclei increases, in upper left corner of Fig.2.9.c. After the relaxation period, the new distance between the molecules is r_2 ($r_2 > r_1$). The electron on the excited state wants to be on more stable energy level, so the emission is detected from nuclei. After the other relaxation period, it complete a cycle diagram about absorption and emission of a defect center.

Figure 2.9.b shows the spectrum from a defect center schematically. The Franck Condon principle is very useful to understand the vibrational-electronic transition. However, line-shape of spectrum from defect centers is needed to a theoretical approach to understand the reason of temperature dependent shifting and broadening of the ZPL.

Firstly, we describe a general Hamiltonian H_i for nuclear motions in a non-degenerate electronic state $|i>$. When the displacement parameter $Q = 0$,

$$H_i = E_i + H_{L0} + H_{Li} \tag{2.13}$$

where E_i is electronic energy of the state, H_{L0} is the Hamiltonian of perfect lattice and H_{Li} involves the nuclear operators to represents electron-phonon interaction and external energies of the system like stress and electric field.

In the linear electron-phonon coupling H_{Li} is written as,

$$H_{Li} = \vec{\varepsilon_i} \cdot \vec{Q} \tag{2.14}$$

where $\vec{\varepsilon_i}$ is a coefficient describes the electron-phonon coupling. The equation 2.14 was written for the perfect lattice. Therefore, we should drive the 'Huang-Rhys factors' S_α for the static distortion in lattice. When the electron translates between states, the position of state changes. The shifting on the nuclei position is an important for the line-shape. The changes on the position for each mode α are defined as,

$$\overline{Q_{j\alpha}} - \overline{Q_{i\alpha}} = q_{ij,\alpha} \tag{2.15}$$

The difference of mean value of final and initial state is described a new displacement factor for H_{Li}.

The Huang-Rhys factor is described as,

$$S_\alpha = S_{\alpha 0} \coth \frac{\hbar\omega_\alpha}{2k_bT} \tag{2.16}$$

where $S_{\alpha 0} = \frac{1}{2}|q_{ij,\alpha}|^2\omega_\alpha^2/\hbar\omega_\alpha$, ω_α is the frequency of each mode, k_b is Boltzmann constant and T is temperature of the sample.

If the Huang-Rhys factor is large, the charge distribution of defects during the transition is not stable. The changes on charge distribution give a form of line-shape. When the Huang-Rhys factor is small, the defect is more stable and the transition on the orbital occurs between far shells of the nuclei like d shell to f shell.

The Huang-Rhys factor is a significant part of Franck Condon principle. During the relaxation period in vibrational-electronic transition in Figure 2.9.a the defects release phonons. The released energy of phonons on relation period is depended on Huang-Rhys factor. The emission of phonon energy is $S_{\alpha 0}\hbar\omega_\alpha$. In the cycle of absorption and emission of defect center Figure 2.9 has two relaxation period. Thus we write the energy conservation of Franck Condon cycle,

$$E_{abs} = E_{em} + 2\hbar\omega_\alpha S_{\alpha 0}. \tag{2.17}$$

If the electron-phonon coupling is weak, Huang-Rhys factor is small and written as,

$$S_0 = \sum_{\alpha} S_{\alpha 0} \tag{2.18}$$

in the limit of weak coupling S_0 is equal to zero and ZPL is seen from the transition of electronic states. If we use the one phonon absorption to make a fit to the function for phonon emission spectrum from defect center. Generally the line-shape is,

$$G(\omega) = G_{ZPL}(\omega) + G_{OPL}(\omega) \tag{2.19}$$

where ω is frequency shift of ZPL, G_{ZPL} is zero phonon line-shape and G_{OPL} is the line-shape of the one phonon approximation. G_{OPL} is consist of two parts with emission (Stokes) and absorption (anti-Stokes) bands.

In the calculation of line-shape function $G(\omega)$, if the method of moments is used, the moment is (Stoneham, 2001);

$$M_N(\overline{\omega}) = \int d\omega G(\omega)(\omega - \overline{\omega})^N \tag{2.20}$$

where $\overline{\omega}$ is arbitrary and M_N is a infinite set of moment with,

$$M_N(\overline{\omega}) = M_N(0) + N M_{N-1}(0)\overline{\omega} + \frac{N(N-1)}{2} M_{N-2}\overline{\omega}^2 + \cdots \tag{2.21}$$

The result of first two moments with using Huang-Rhys model is

$$\hbar M_1(\omega_{ij}) = 0 \tag{2.22}$$

$$\hbar^2 M_2(\omega_{ij}) = S(\hbar\omega_0)^2(2n+1) \tag{2.23}$$

When the number of N in M_N is higher than three, Huang Rhys factor increases. In the second moment the line shape becomes Gaussian. Therefore, the FWHM Γ is depended on the second moment;

$$\Gamma^2 = 8\ln(2)\hbar^2 M_2 \tag{2.24}$$

The measured linewidth with line shape function is,

$$\Gamma_m = \sqrt{8ln(2)\hbar^2 \frac{\int \omega^2 G(\omega) d\omega}{\int G(\omega) d\omega} + R^2} \tag{2.25}$$

where R is resolution of the device.

Jungwirth et al. (2016) is consisted of a theoretical model to understand the line shape of emission from hBN defect centers. They used weak coupling approximation Eq.2.18 for one phonon line shape function G_{OPL} with,

$$G_{OPL}(E) = \frac{cg(E)f(E)}{\exp(\frac{E}{k_BT}) - 1} \tag{2.26}$$

where $g(E)$ is phonon DOS and $f(E)$ is the defect phonon coupling. When they used low energy phonon limits (Fig.2.17), they found the fitting function of measured line width as,

$$\Gamma_M = \sqrt{8ln(2)\frac{\int E^{2+n}dE/\left[\exp\frac{E}{k_BT} - 1\right]}{A\exp\left[-S\coth(\Delta E/4Sk_BT)\right] + \int E^n dE/\left[\exp\frac{E}{k_BT} - 1\right]} + R^2}$$

In this fitting function Jungwirth et al. (2016) only studies on one phonon approximation. Additionally, Exarhos et al. (2017) worked on the functional form of the n-phonon contributions to the PSB and showed how to the line shape on emission from hBN defect center.

2.4.4. Experimental Results

In the last part, theoretical approach for line shape of ZPL emission with temperature dependence is discussed. In this part, we discuss temperature dependence experimental results. This part of the section is included representation of temperature series data analyzes. Several experiments have successfully employed defect center on multilayer hBN flakes with μPL setup (Figure 2.1). Linkam THMS600$^{\mathbf{TM}}$ that is liquid nitrogen cryostat, is used to temperature control of hBN sample and Olympus LMPLFLN50x$^{\mathbf{TM}}$ is preferred at low temperature experiments, due to focal length, is 10.6 mm. Additionally, the hBN defects is excited with 488 nm laser.

In data analysis, Pseudo voigt model is used for calculation of linewidth of PL spectrum,

$$f = \frac{(1-\alpha)A}{\Gamma_g\sqrt{2\pi}}e^{|-(x-\mu)^2/2\Gamma_g^2|} + \frac{\alpha A}{\pi}[\frac{\Gamma}{(x-\mu)^2 + \Gamma}] \tag{2.27}$$

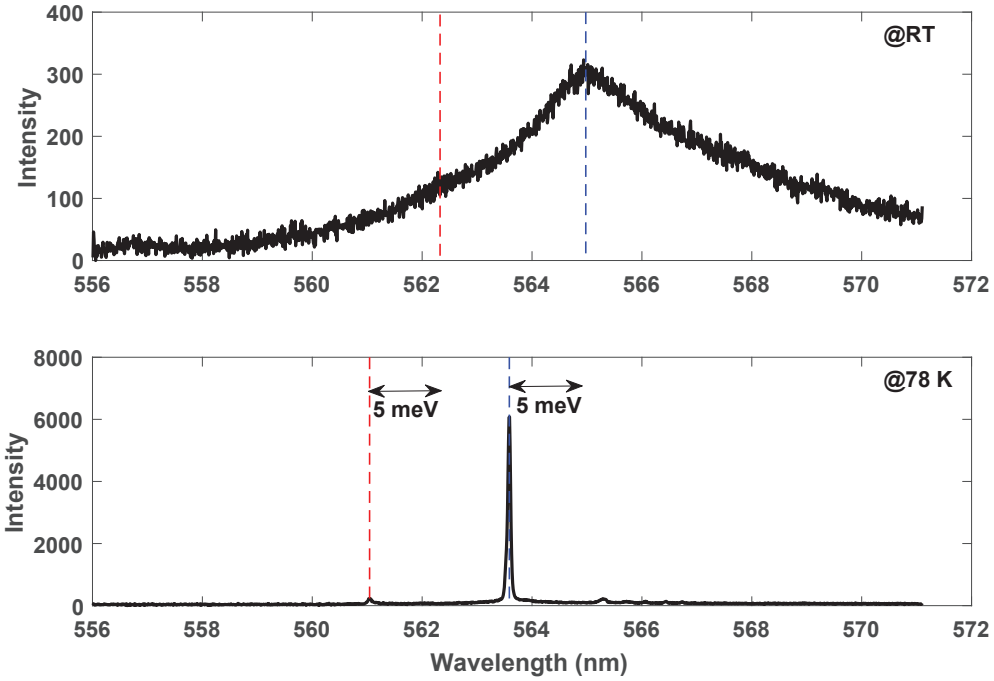

Figure 2.10. Upper figure is about a ZPL emission from hBN defect center at room temperature, lower figure is ZPL emission from same defect center at 78 K. The blue dashes represent the ZPL emission wavelength and the red dashes are acoustic phonons emission wavelength

the left part of Eq.2.27 describes Gaussian model and right part includes Lorentzian components. In Eq.2.27, A is an amplitude, μ is center point of spectrum, Γ_g is equal to $\Gamma/\sqrt{2\ln 2}$, 2Γ is full width half maximum (FWHM) and α is a fraction to control the rate of Gaussian and Lorentzian models.

The temperature of sample directly effects the broadening of ZPL. The key point of linewidth of ZPL emission is the level of phonon vibrations because acoustic phonons are located near the electronic states. The upper part of Fig.2.10 is a room temperature data from hBN defect center. Its line shape is broad due to phonon vibration. When the temperature decreases, phonons in high energy levels begin to come in more stable energy states. Therefore, the rate of phonon vibration is decreasing with temperature and the FWHM of ZPL emission is decreasing. The lower part of Figure 2.10 is a basic example of reducing on FWHM due to temperature dependence of phonons vibrations and also 20 times increasing on intensity of ZPL emission is shown at Figure 2.10.

The other important effect of phonons is temperature-dependent energy shift. In Figure 2.11 two different representation of energy shift on ZPL emission from hBN defect

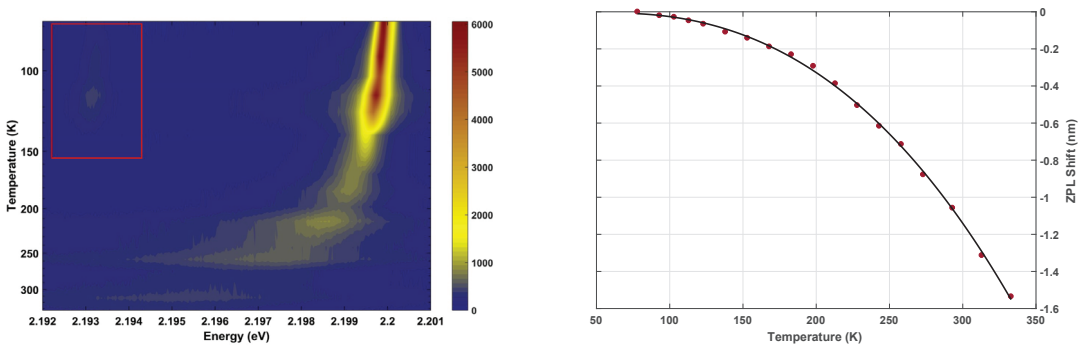

Figure 2.11. In the left part of figure each temperature is plotting with color map and the red rectangle emphasizes the acoustic phonons. The right part of figure shows center of emission shifts.

center. The left part of Figure 2.11 is consisted of ZPL emission spectrum that measured at 17 different temperatures from same hBN defect center. Additionally, the z direction of the figure represents the intensities of ZPL emissions. In the left part of Figure 2.11 energy shift depended on temperature is easily seen that energy change is 2.199 to 2.194 eV. The right part of Figure 2.11 is direct representation of energy shift with wavelength. The changes ZPL emission wavelength centers trend is T^3.

The Figure 2.10 and 2.11 are described the acoustic phonon lines. In the Figure 2.10 red dashes (at 562.2 and 562 nm) are the high energy level acoustic phonons to ZPL energy, left part of Figure 2.11 shows the lower energy acoustic phonons. At room temperature spectrum, acoustic phonons distorts the line shape symmetry and creates a shoulder on low energy part of the spectrum. The displacement of energy level between ZPL and lower energy acoustic phonon is $\sim$7 meV and on higher energy acoustic phonon is $\sim$10 meV. The temperature-dependent energy shift in a acoustic phonon is similar to ZPL energy shift as $\sim$5 meV.

The resolution of the device delimits the measured linewidth. Therefore, we use a method to improve the resolution of measured data. The method is deconvolution computing with two different Fourier transform. Firstly, the measured minimum linewidth (excitation laser) approximate to equal zero and calculating rate of Fourier transform. Secondly, the rate is applied to all raw data with inverse Fourier transform. Finally, the linewidth of deconvoluted data is calculated with Pseudo voigt model. The left part of Figure 2.12 shows the difference raw and deconvoluted data. The raw data is represented with black square and the deconvoluted data is shown with red circles in the left part of

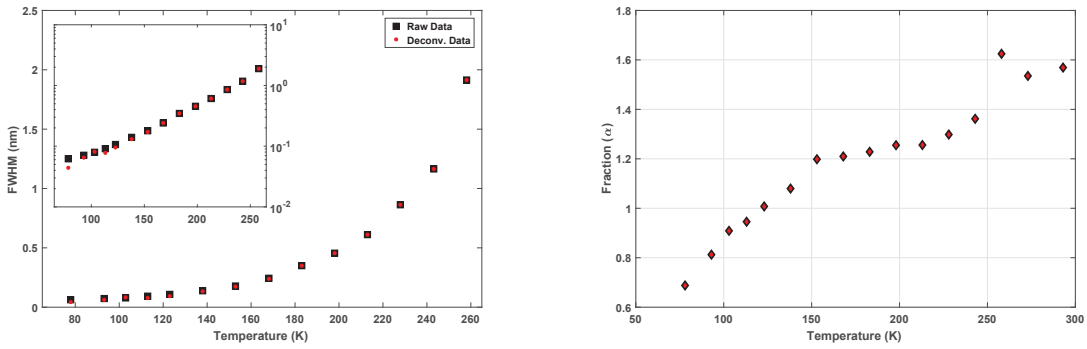

Figure 2.12. The left part of figure is linewidth changes of raw and deconvoluted data on linear and logarithmic scale. The right part of figure shows that Gaussian and Lorentzian rate of ZPL with Pseudo voigt model fitting.

Fig.2.12. At the high temperature the deconvoluted data is similar with raw data but at the low temperature, the resolution of device is not enough to measure the real linewidth. At 78 K linewidth of raw data is 0.062 nm but deconvoluted data has more smaller linewidth is 0.044 nm.

The right part of Figure 2.12 is fraction that emphasize rate of Gaussian and Lorentzian components in Eq.2.27. According to the fraction figure (2.12), the line shape on ZPL emission from hBN defect center has more Gaussian components at low temperature, but the Lorentzian shape is more dominant at high temperature.

2.5. Statistics

The main purpose on this part of the thesis is the distribution of emission lines from defect centers on hBN flakes. Moreover, electronic density of states of hBN defect centers will be studied. The statistical experiment on 630 distinct defects in 47 multilayer hBN flakes is investigated. During the experiment, motorize x-y stage and 532 nm excitation laser on μPL set-up (Fig.2.1) are employed. One by one 47 mapping with $\sim$1mW (after the ND filter on μPL set-up) excitation laser power was done. We used more power than saturation power to excite the deep defects.

Figure 2.13 shows the distribution of emission lines with energy difference from 532 nm (2.33 eV) excitation laser. The red dashes with 169 meV energy parts describe the electronic states in Fig.2.9.a and describe the more probable absorption and emission

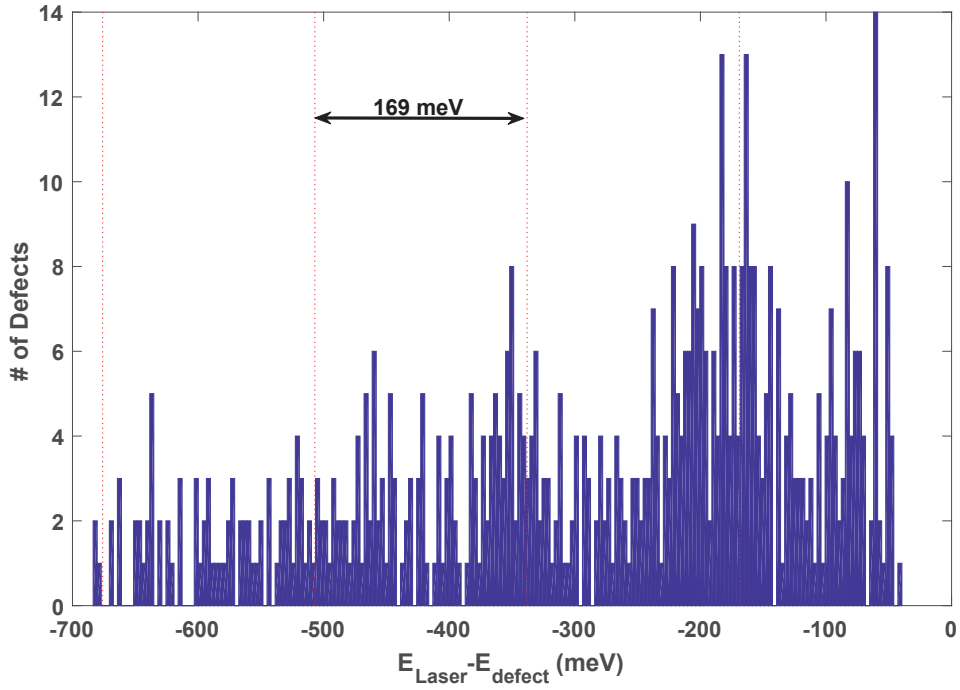

Figure 2.13. The histogram of line position of defect centers with energy difference from excitation laser energy. The red dashes show that each 169 meV differnce from laser.

lines thus clustering near the dashes is shown in Fig.2.13. In normal circumstances, ZPL from hBN may emits on all wavelengths which energies are less than excitation laser, but according to the excitation laser energy, some defects may not be excited due to phonon DOS. The phonon DOS of ultraviole (UV) hBN color center was recorded with some gaps in energy detuning in Vuong et al. (2016). We do not work on UV defect center, but same gaps can be seen in Fig.2.13. Additionally, Figure 2.b in Jungwirth et al. (2016) has a gap in $\sim$2.08 eV on hBN flakes. The our statistical data from hBN defects is not enough to determinate phonon DOS but it gives a hint for band diagram of defects.

Figure 2.14 shows relative line intensity of same defects in Fig.2.13 in logarithmic scale. The intensity distribution of each emission line has a diminishing trend. The same clustering in Fig.2.13 is detected. Moreover, linearly decreasing on Fig.2.14 is observed, because the probability of electronic states transition diminishes with energy difference from excitation laser.

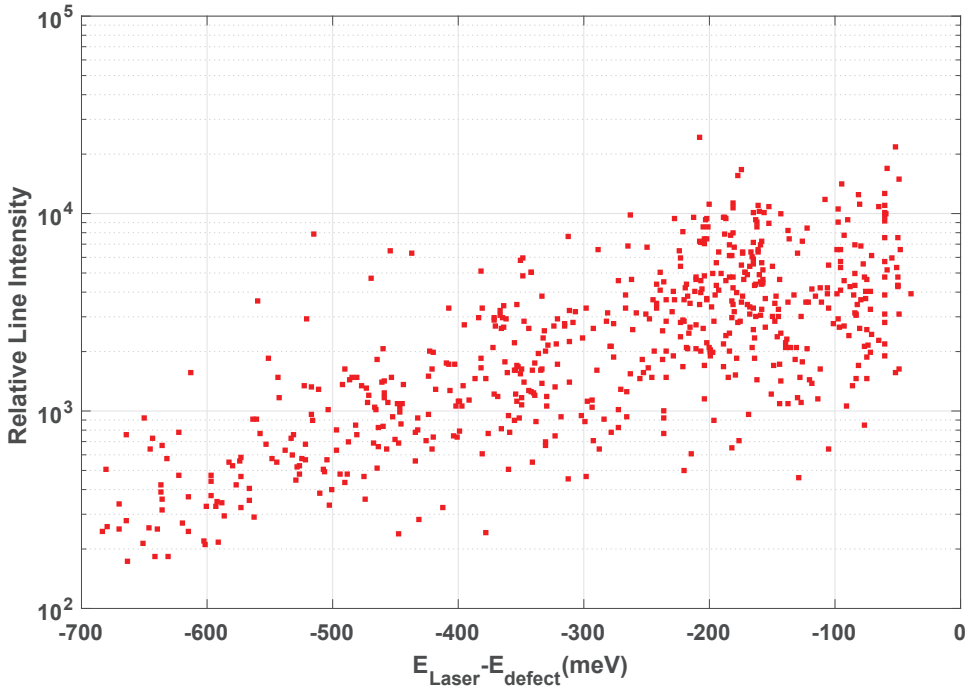

Figure 2.14. The individual emission lines have differnt brigthness.

2.6. Conclusion

This chapter of thesis was studied on temperature dependence ZPL emission from hBN defect center.

In first section, we explain the historical development of optical properties of 2D and bulk hBN.

In the second section, the experimental set-up was explained with details and we described our experimental infrastructures in the laboratory.

The third section is consisted of basic description of Raman and PL spectroscopy. Raman spectroscopy was used to determine that hBN on the substrate and Raman shifts was recorded as 1365 cm^{-1}. The physical background of ZPL emission with photon emission was discussed.

In the fourth section, the basic optical properties of hBN defect centers were investigated with power and polarization series. Therefore, we showed that ZPL on hBN color centers is emitted from quantized states with $\sim$0.5 mW saturation power and $\sim$90% polarization dependence visibility.

The fifth section is the main part of the chapter. The temperature dependence of

hBN defect centers was investigated with a theoretical model. The line shape of ZPL emission is affected from electron phonon interaction and it explains with Huang Rhys factor. The experimental results describe the acoustic and optical phonons with shifts on ZPL centers and linewidth changes.

The last section of the chapter is consisted of statistical study on emission lines on hBN defects. We investigated on the distribution ZPL emissions and showed clustering on each 169 meV energy difference from excitation laser.

Finally, hBN is a solid-state single photon emmiter based on defects, because of the emission from quantized states. The line shape broadening of ZPL is directly effected from temperature due to vibrational phonons. Eventually, hBN is a single photon source work on at room temperature.

CHAPTER 3

DESIGN OF PHOTON-PAIR SOURCE

In the past several decades, nonlinear optical crystals which are beta-barium borate (BBO) (Kwiat et al., 1995) and potassium titanyl phosphate (KTP) (Sanaka et al., 2001), have been used to photon pair generation but these materials are not suitable for chip technology. An important obstacle to chip scale photon pair generation was achieved with periodically poled lithium niobate (PPLN) (Tanzilli et al., 2002). These materials have second order susceptibility ($\chi^{(2)}$), thus spontaneous parametric down conversion (SPDC) process is applied to photon pair generation. After the evolution of silicon technology, the silicon based waveguides were the popular materials to chip scale waveguide (Takesue, 2012). Silicon based materials have third order susceptibility ($\chi^{(3)}$) ,so four wave mixing (FWM) process can be used to photon pair generation. The silicon based materials is not only used in FWM process, but also used in second harmonic generation (Cazzanelli et al., 2011), third harmonic generation (Ning et al., 2013), frequency conversion (Agha et al., 2012) and etc. Moreover, silicon nitride that has more available range (780-1550 nm), is a new material in chip scale waveguide to photon pair generation. In the thesis, we prefered silicon nitride waveguide to photon pair generation because the waveguide is an avaliable photon pair source in visible band.

This chapter is consisted of two main subtopic. First one is electromagnetic wave calculation to decide a waveguide geometry. Second one is nonlinear effects in silicon nitride waveguide and applying four wave mixing process to integrated waveguide.

3.1. Waveguide Theory

Maxwell's equations represent secrets and limits of electromagnetism and optics, and consist of four equations;

$$\nabla \times \mathbf{E} + \frac{\partial \mathbf{B}}{\partial t} = 0 \tag{3.1}$$

$$\nabla \times \mathbf{H} - \frac{\partial \mathbf{D}}{\partial t} = \mathbf{J} \tag{3.2}$$

$$\nabla \cdot \mathbf{D} = \rho \tag{3.3}$$

$$\nabla \cdot \mathbf{B} = 0 \tag{3.4}$$

where $\mathbf{E}$ (V/m) and $\mathbf{H}$ (Amps/m) are amplitudes of electric fields and magnetic fields, $\mathbf{D}$ (C/m^2) and $\mathbf{B}$ (Wb/m^2) describe electric and magnetic flux densities and also ρ (Amps/m^2) $\mathbf{J}$ (C/m^3) are densities of charge and current.

$\mathbf{E}$ and $\mathbf{H}$ describe a amplitude that show effects of a given point in space to a field. However, $\mathbf{D}$ and $\mathbf{B}$ explain a flux density.In a isotropic(homogeneous) media, between the field amplitude and flux density in electromagnetism have a relation that;

$$\mathbf{B} = \mu \mathbf{H} \tag{3.5}$$

$$\mathbf{D} = \epsilon \mathbf{E} \tag{3.6}$$

with ϵ (Farads/m) is electric permittivity of medium and μ (Henrys/m) is magnetic permeabilty of medium. In linear medium, ϵ and μ do not affect the field term. Otherwise, in vacuum ,permittivity and permeabilty are desribed ϵ_0 and μ_0 and values are;

$$\epsilon_0 = 8.854 \cdot 10^{-12} \text{ Farads/m}$$

$$\mu_0 = 4\pi \cdot 10^{-7} \text{ Henrys/m}$$

3.1.1. The Wave Equation

The electromagnetic wave has some condition that must be satisfied source free, linear and isotropic medium in Maxwell's equations. The mean of source free is that ρ and $\mathbf{J}$ are zero. Maxwell's equations in electromagnetic waves are;

$$\nabla \times \mathbf{E} = -\frac{\partial \mathbf{B}}{\partial t} \tag{3.7}$$

$$\nabla \times \mathbf{H} = \frac{\partial \mathbf{D}}{\partial t} \tag{3.8}$$

$$\nabla \cdot \mathbf{D} = 0 \tag{3.9}$$

$$\nabla \cdot \mathbf{B} = 0 \tag{3.10}$$

for the calculation of wave equation. We start the calculation from curl of Eq(3.7) with 3.5 and 3.6, we will reach

$$\nabla \times \nabla \times \mathbf{E} = -\mu\epsilon \frac{\partial^2 \mathbf{E}}{\partial t^2} \tag{3.11}$$

and also continue with a vector calculation rule $\nabla \times \nabla \times \mathbf{A} = \nabla(\nabla \cdot \mathbf{A}) - \nabla^2 \cdot \mathbf{A}$. In homogeneous and linear medium, the wave equation for electric field is

$$\nabla^2 \mathbf{E} - \mu\epsilon \frac{\partial^2 \mathbf{E}}{\partial t^2} = 0 \tag{3.12}$$

and also do similar calculation for magnetic field, the wave equation is

$$\nabla^2 \mathbf{H} - \mu\epsilon \frac{\partial^2 \mathbf{H}}{\partial t^2} = 0 \tag{3.13}$$

3.2. Optical Waveguides

The infinite slab waveguide that is a basic example to the optical waveguides, may be used to understand essential properties of the waveguides. Fig 3.1 is one dimensional slab waveguide that consist of three different materials with two main mediums core and cladding and refractive index of core must be larger than cladding indexes ($n_f > n_s, n_c$).

The way of electromagnetic wave starts from left side of the core and continue with reflections inside the core and so the propagation direction is $\hat{z}$ axis. When optical waves propagate a limiting mediums, transverse modes that are TE (transverse electric) and TM (transverse magnetic) are observed. TE mode does not have electric field at $\hat{z}$ axis and TM mode does not have magnetic field at $\hat{z}$ axis.

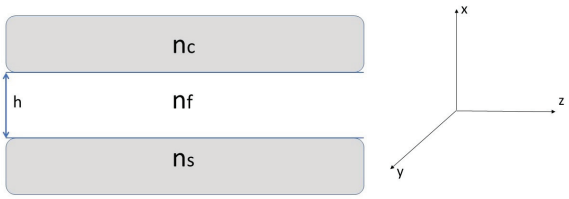

Figure 3.1. The planar slab waveguide with three materials that have different refractive indexes and the slab is finite in x direction but infinite in y and z directions.

If the Eq.3.12 is rewritten for vacuum;

$$\nabla^2 E_y + k_0^2 n_i^2 E_y = 0 \tag{3.14}$$

with $|k_0| = \frac{\omega_0}{c}$ and k_0 describes the vacuum wave vector, ω_0 is source frequency and in TE mode, electric filed ($E_y(x,z)$) only polarized at $\hat{y}$ direction, also $n_i = n_f$ or n_s or n_c.

The optical wave propagates two different directions, so $E_y(x,z)$ is function of x and z directions. We can decide $\hat{z}$ direction the phase variable, because of main propagation in $\hat{z}$ direction.

$$E_y(x,z) = E_y(x)e^{-i\beta_i z} \tag{3.15}$$

where β is propagation coefficient at the $\hat{z}$ direction.

The new version of wave equation is ;

$$\frac{\partial^2 E_y}{\partial x^2} + (k_0^2 n_i^2 - \beta^2)E_y = 0 \tag{3.16}$$

where n_i is depend on height ($n_i(x)$). Therefore, changes in position x refers to different refractive indexes. $n_i(x) < 0$ subsumes n_s , $0 < n_i(x) < h$ covers n_f values and otherwise shows that n_c (Fig 3.1).

In Eq 3.16, $k_0^2 n_i^2 - \beta^2$ creates different types of solutions from the differential equation of electric filed. First case is $k_0^2 n_i^2 - \beta^2 > 0$ that gives an oscillatory wave solution.

$$E_y(x) = A\sin(\sqrt{k_0^2 n_i^2 - \beta^2}x) + B\cos(\sqrt{k_0^2 n_i^2 - \beta^2}x) \tag{3.17}$$

where A and B are constant. The second case is $k_0^2 n_i^2 - \beta^2 < 0$ that gives real exponential solution and the part of the wave includes evanescent field.

$$E_y(x) = Ae^{\pm\sqrt{\beta^2 - k_0^2 n_i^2}x} \tag{3.18}$$

In first case, $\sqrt{k_0^2 n_i^2 - \beta^2}$ can be defined a transverse wavevector (κ), so the electric field for oscillatory wave part is written as $E_y(x) = A\sin(\kappa x) + B\cos(\kappa x)$. In second case, $\sqrt{\beta^2 - k_0^2 n_i^2}$ can be defined attenuation coefficient (γ), so the electric field for evanescent wave part is written as $E_y(x) = Ae^{\pm\gamma x}$

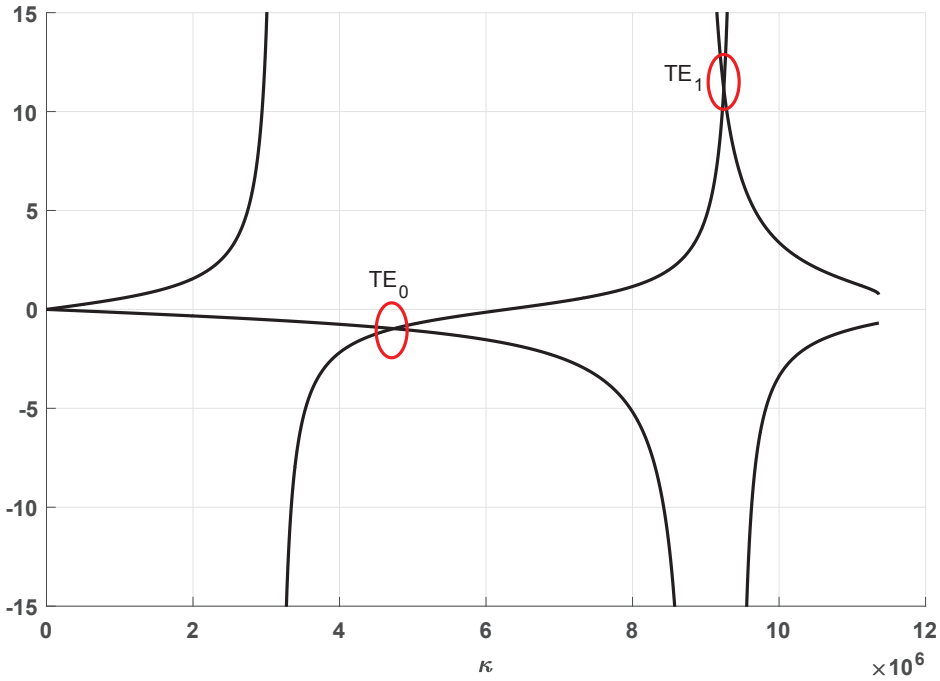

Figure 3.2. Number of TE mode calculation result with wavelength 780 nm and height 500 nm

β is the longitudinal wavevector that is the main parameter for mode solutions and we need to decide boundaries of β. If we assume that $n_s \geq n_c$, β must be greater than $k_0 n_s$ (if $k_0 n_s > \beta$, the wave does not propagate in waveguide and it never satisfies total internal reflection process), and the same reason is acceptable for $k_0 n_f < \beta$. Consequently, the boundary condition of β is ;

$$k_0 n_s < \beta < k_0 n_f \tag{3.19}$$

For the mode solution, the boundary conditions for β adapt for electric field ;

$$E_y(x) = Ae^{\gamma_c(x+h)} \qquad x > h \tag{3.20}$$

$$E_y(x) = B\sin(\kappa x) + C\cos(\kappa x) \qquad 0 < x < h \tag{3.21}$$

$$E_y(x) = Ae^{\gamma_s x} \qquad x < 0 \tag{3.22}$$

The boundary conditions must satisfy two main process that tangential electric field and magnetic field are continuous. The results of boundary condition solutions give the number of TE modes from eigenvalue of β;

$$\tan(h\kappa) = \frac{\gamma_s + \gamma_c}{\kappa(1 - \frac{\gamma_s\gamma_c}{\kappa^2})} \tag{3.23}$$

The Fig 3.2 is basic example of number of TE modes for h equals to 500 nm and wavelength is 780 nm. Firstly, we calculate κ and γ's with specific h and λ and plot the left part and right part of Eq 3.2.2 separately. The number of junction of two graphs is equal to the number of TE modes. In Fig 3.2, we have two TE modes, so first mode is TE_0 and second is TE_1.

If we do same calculations for TM modes, the eigenvalue of β for magnetic field is,

$$\tan(h\kappa) = \frac{\kappa(\frac{n_f^2}{n_s^2}\gamma_s + \frac{n_f^2}{n_c^2}\gamma_c)}{\kappa^2 - \frac{n_f^4}{n_c^2 n_s^2}\gamma_s\gamma_c} \tag{3.24}$$

3.2.1. Strip Waveguide

The strip (or ridge) waveguide is a basic and popular optical waveguide and also it is useful for real three dimensional waveguide calculation.

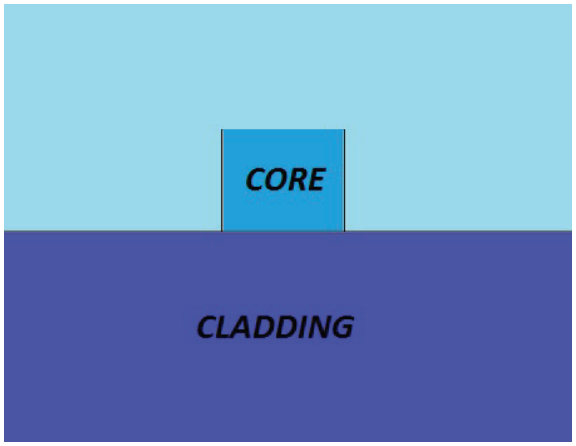

Figure 3.3. Simple example of strip waveguide with core, cladding and upper part is air.

Figure 3.3 is basic description of the strip waveguide. The advantage of the waveguide is available for basically using effective index method that gives an analytic so-

lutions. The slab waveguides consisted of n_f, n_s and n_c refractive indexes, but strip waveguides have n_{eff} that is effective refractive index, and $n_{cladding}$ that is refractive index of cladding (upper part is air). The laser coupling efficiency of the core in the waveguide may easily be calculated with n_{eff} in the mode calculations. The coupling efficiency will be discussed in 'Dispersion Engineering' section of the chapter.

COMSOL Multiphysics® is a software for simulating for scientific and engineering problems and consisted of many modules to simulate the physics experiments and design the sample. The Wave Optics Module is used for electromagnetic wave propagation in linear and nonlinear optical media and the module is available for simulation and optical design optimization in the waveguides.

In this thesis COMSOL Multiphysics® was used for the basic properties of the optical modes for silicon nitride optical waveguide. The mode solutions for a typical silicon nitride waveguide will be discussed in the next section.

3.2.2. Mode Solutions

In this section we focus on optical modes for silicon nitride waveguide and discuss how to appear TE and TM modes in a specific waveguide core. Here, we define a strip waveguide with silicon dioxide cladding and silicon nitride core which weight is 650 nm and height is 500 nm, and consider a wavelength of 780 nm.

Figure 3.4 indicates the electric field distribution of the first four optical modes. COMSOL Multiphysics® is used to finite element (FEM) solvers for optical mode and effective refractive index (n_{eff}) calculations. Figure 3.4.a is TE_{00} mode with $n_{eff} = 1.85$, figure 3.4.b shows TM_{00} modes and n_{eff} is 1.84, figure 3.4.c describes TE_{10} mode with $n_{eff} = 1.64$ and figure 3.4.d is TM_{10} mode and n_{eff} is 1.59. TE and TM modes polarize in two different directions that are easily shown in Figure 3.4.c and d. TE modes polarized in x-direction but TM modes polarized in y-direction.

The other important results of mode solutions with COMSOL Multiphysics® is effective mode area that shows the confinement of electric field on waveguide. The details and calculations will be discussed in 'Third Order Nonlinear Effects' section.

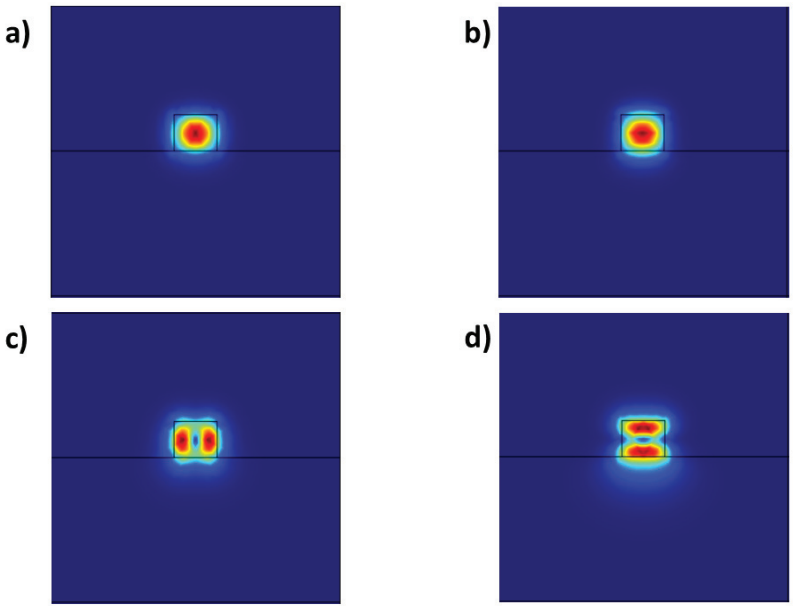

Figure 3.4. Electric field distribution for a) TE_{00}, b) TM_{00}, c) TE_{10} and d) TM_{10}

3.3. Dispersion Engineering

When the light is confined a waveguide, it travels with different speeds. Thus, the propagation velocity is $v_p = \frac{\omega}{k}$ and $v_p = \frac{c}{n}$ can be described under the uniform dielectric. If we redefine the equation with effective refractive index,

$$v_p = \frac{\omega}{\beta} = \frac{c}{n_{eff}} \tag{3.25}$$

where β is propagation constant at z direction and c is the speed of light.

The speed of light depends on the frequency of wavelength when the light is propagated a dielectric medium. The different velocity affects the refractive index of the medium and it can be described with Sellmeier equation;

$$n^2(\lambda) = 1 + \sum_i \frac{A_i \lambda^2}{\lambda^2 - B_i^2} \tag{3.26}$$

where λ is wavelength of light. Luke et al. (2015) gives Sellmeier equation coefficients for Si_3N_4 and also Malitson (1965) gives the coefficients for SiO_2.

Figure 3.5 shows the changes on refractive indices. $n_{Si_3N_4}$ and n_{SiO_2} is calculated

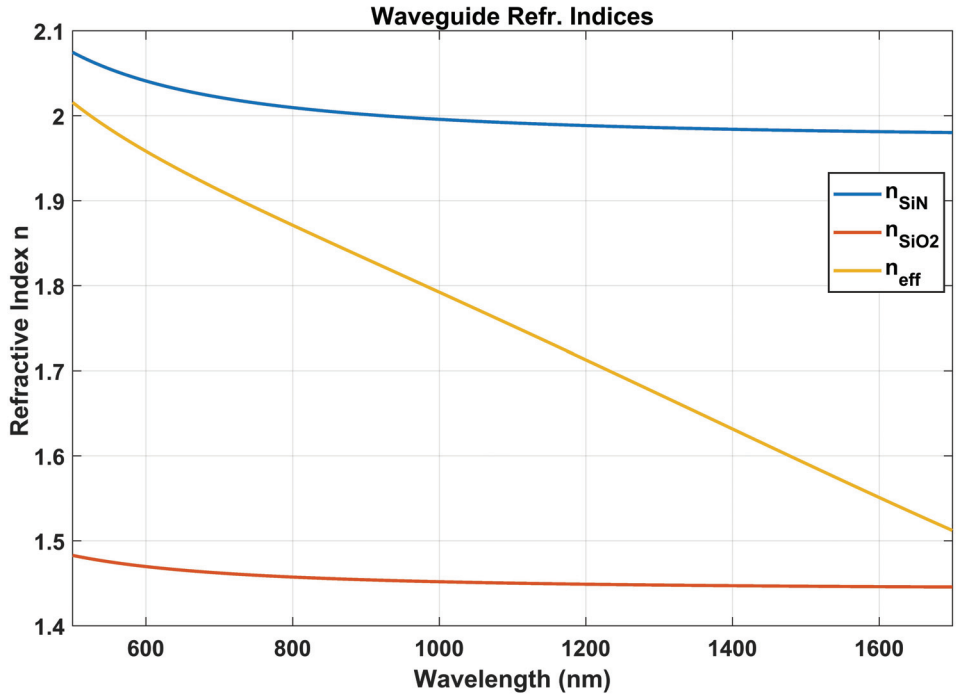

Figure 3.5. The variations of refractive indices of core (Si_3N_4) and cladding (SiO_2) of waveguide and effective refractive index depend on wavelength

with Sellmeier equation but n_{eff} is determined with COMSOL Multiphysics®. Additionally, figure 3.5 verifies $n_{Si_3N_4} > n_{eff} > n_{SiO_2}$.

Equation 3.25 shows that propagation coefficient represents the dependence with n_{eff};

$$\beta(\omega) = n_{eff}(\omega)\frac{\omega}{c}. \tag{3.27}$$

The propagation constant can be defined with Taylor series;

$$\beta(\omega) = \beta_0 + \beta_1(\omega - \omega_0) + \frac{1}{2}\beta_2(\omega - \omega_0)^2 + \frac{1}{3!}\beta_3(\omega - \omega_0)^3 + \cdots \tag{3.28}$$

where β_i's define the i-th order dispersion with $\beta_i = \left(\frac{d^i\beta}{d\omega^i}\right)_{\omega=\omega_0}$.

The first order dispersion is related to group velocity (v_g) and index (n_g). This is defined as;

$$\beta_1 = \frac{1}{v_g} = \frac{n_g}{c} = \frac{1}{c}\left(n_{eff} + \omega\frac{dn_{eff}}{d\omega}\right). \tag{3.29}$$

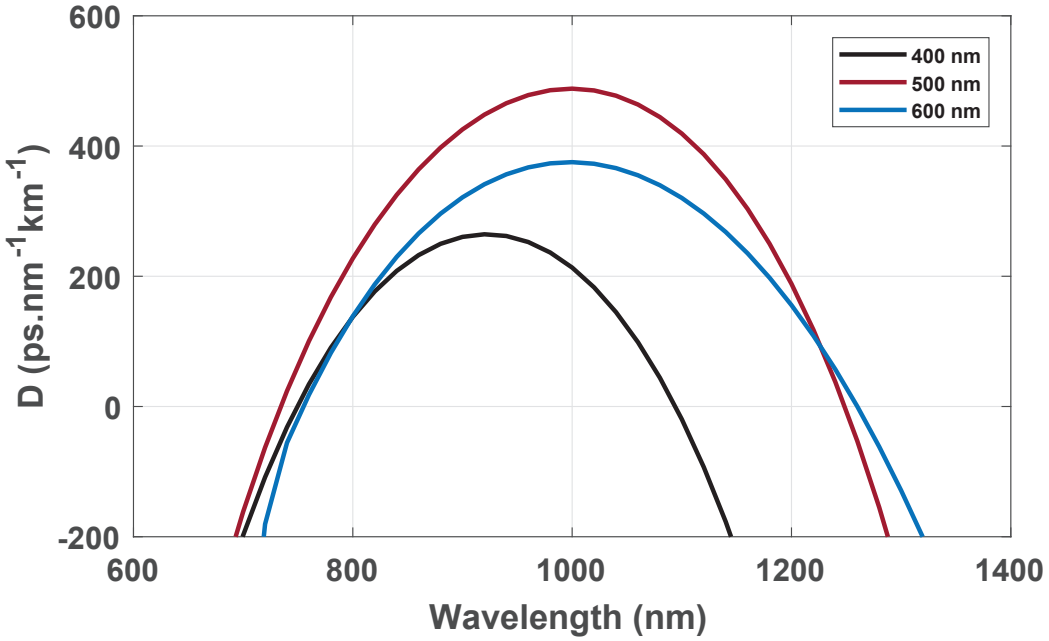

Figure 3.6. Dispersion calculation with a specific width is 650 nm and the height changes with 400 to 600 nm

The second order dispersion parameter is directly related with group velocity dispersion (GVD) from $\beta_2 = \frac{d\beta_1}{d\omega}$ and it written as;

$$\beta_2 = \frac{1}{c}\left(2\frac{dn_{eff}}{d\omega} + \omega\frac{d^2n_{eff}}{d\omega^2}\right). \tag{3.30}$$

Additionally, the dispersion is defined as;

$$D = -\frac{\lambda}{c}\frac{d^2n_{eff}}{d\lambda^2}. \tag{3.31}$$

In this thesis, the main purpose of calculation the dispersion is determination of size of waveguide for a specific wavelength which gives that second order dispersion is equal to zero. This wavelength is known as zero dispersion wavelength (ZDW).

In Figure 3.6 we show the calculation of dispersion as a function of wavelength for the TE_{00} mode. In the calculation, Si_3N_4 core width of the waveguide is fixed at 650 nm and height is chosen three different size (400 nm, 500 nm, 600 nm). When the size of core 650×600 nm^2, the blue one in Fig.3.6, has ZDW near the wavelength as 780 nm. Here, we decided the size of the our Si_3N_4 core with SiO_2 cladding, the next point is calculation of nonlinear effects and we will discuss it in the next section.

3.4. Nonlinear Effects

In the last section we found a specific waveguide size (650×600 nm^2) with dispersion engineering. In this section we investigate nonlinear third order susceptibility and we calculate third order nonlinear effects for integrated silicon nitride waveguide.

3.4.1. Susceptibility

The part of section is consisted of calculation of susceptibility to understand of the nonlinear interactions on an atom.

The calculation is began from a general Hamiltonian operator with atomic wave function $\Psi(\mathbf{r}, t)$ which has been solved with time-dependent Schröndiger equation. The Hamiltonian operator is

$$\hat{H} = \hat{H}_0 + \hat{H}_{int} \tag{3.32}$$

where $\hat{H}_0$ is a free atom Hamiltonian and interaction Hamiltonian which represents the interaction between atom and electromagnetic field, is $\hat{H}_{int}$. The electric dipole moment operator $\hat{\mu}$ is used for description of interaction;

$$\hat{H}_{int} = -\hat{\mu} \cdot \mathbf{E}^{'}(t) \tag{3.33}$$

where $\hat{\mu} = -e\hat{r}$ and $-e$ is the charge of the electron. $\mathbf{E}^{'}(t)$ represents the discrete summation of frequency components with $\mathbf{E}^{'}(t) = \sum_i \mathbf{E}(\omega_i) e^{-i\omega_i t}$.

If the state vector is written with phase factor, it is

$$\Psi_n(\mathbf{r}, t) = \psi_n(\mathbf{r})\, e^{-i\omega_n t}. \tag{3.34}$$

The time independent state vector $\psi_n(\mathbf{r})$ is created a basic road for the calculation of susceptibility. The eigenvalues of state vector are satisfied and have complete and orthonormal sets.

The Hamiltonian of interaction between electromagnetic field and an atom cannot be solved exactly. Therefore, we need to perturbation theory to solve the Schröndiger equation. The Equation 3.32 is replaced to apply perturbation theory by

$$\hat{H} = \hat{H}_0 + \lambda \hat{H}_{int}(t) \tag{3.35}$$

where λ is a parameter that describes the strength of the interaction. Additionally, λ is a small parameter, thus the eigenstates is written as a taylor series,

$$\Psi_n(\mathbf{r}, t) = \Psi_n^{(0)}(\mathbf{r}, t) + \lambda \Psi_n^{(1)}(\mathbf{r}, t) + \lambda^2 \Psi_n^{(2)}(\mathbf{r}, t) + \cdots \tag{3.36}$$

The Schröndiger equation ($i\hbar \frac{\partial \psi}{\partial t} = \hat{H}\psi$) is written for Equation 3.35;

$$i\hbar \frac{\partial \Psi^{(N)}}{\partial t} = \hat{H}_0 \psi^{(N)} + \hat{H}_{int} \Psi^{(N-1)} \tag{3.37}$$

where $N = 1, 2, 3 \cdots$ and if $N = 0$, the Schröndiger equation describes only free atom without interaction: $i\hbar \frac{\partial \Psi^{(0)}}{\partial t} = \hat{H}\Psi^{(0)}$.

The general wavefunction with Nth-order contribution and $c_l(t)$ probability amplitude is

$$\Psi^{(N)}(\mathbf{r}, t) = \sum_l c_l^{(N)}(t) \psi(\mathbf{r}) e^{-i\omega_l t} \tag{3.38}$$

where l represents the energy eigenstate of atom at time t. The probability coefficient is calculating to using with orthonormal properties,

$$c_m^{(N)}(t) = \frac{1}{i\hbar} \sum_l \int_{-\infty}^{t} dt' V_{ml}(t') c_l^{(N-1)}(t') e^{i\omega_{ml} t'} \tag{3.39}$$

where $V_{ml} = \langle m | \hat{H}_{int} | l \rangle$ and c_m comes from orthonormality. According to $N = 1, 2, 3$, $c_m^{(N)}$ is interested in linear, second order, third order susceptibilities. $c_m^{(3)}$ for third order susceptibility is given by

$$\begin{aligned} c_v^{(3)}(t) &= \frac{1}{\hbar^3} \sum_{pqr} \sum_{mn} \frac{\left[\mu_{vn} \cdot \mathbf{E}(\omega_r)\right] \left[\mu_{nm} \cdot \mathbf{E}(\omega_q)\right] \left[\mu_{mg} \cdot \mathbf{E}(\omega_p)\right]}{\left(\omega_{vg} - \omega_p - \omega_q - \omega_r\right) \left(\omega_{ng} - \omega_p - \omega_q\right) \left(\omega_{mg} - \omega_p\right)} \\ &\times \quad e^{i(\omega_{vg} - \omega_p - \omega_q - \omega_r)t} \end{aligned} \tag{3.40}$$

The general expectation of the electric dipole moment is

$$\langle p \rangle = \langle \Psi | \hat{\mu} | \Psi \rangle \,. \tag{3.41}$$

The expectation value of dipole moment per atom for the calculation of third order susceptibility is written as,

$$\left\langle p^{(3)} \right\rangle = \left\langle \Psi^{(0)} | \hat{\mu} | \Psi^{(3)} \right\rangle + \left\langle \Psi^{(1)} | \hat{\mu} | \Psi^{(2)} \right\rangle + \left\langle \Psi^{(2)} | \hat{\mu} | \Psi^{(1)} \right\rangle + \left\langle \Psi^{(3)} | \hat{\mu} | \Psi^{(0)} \right\rangle . \quad (3.42)$$

The result of expectation value of dipole moment per atom is written as summation of ω_p, ω_q and ω_r with positive, negative combinations in denominator part of Equation 3.40. ω_p, ω_q and ω_r represent the transitions frequency between the quantum states of atom.

Here we need to nonlinear polarization $\widetilde{\mathbf{P}}$ to calculate third order susceptibility $\chi^{(3)}$. The relation between dielectric polarization $\mathbf{P}$ and susceptibility written as,

$$\mathbf{P} = \epsilon_0 \left(\chi^{(1)} \cdot \mathbf{E} + \chi^{(2)} \cdot \mathbf{EE} + \chi^{(3)} \cdot \mathbf{EEE} + \cdots \right) . \quad (3.43)$$

The relation between nonlinear polarization and dielectric polarization is generally described with,

$$\widetilde{\mathbf{P}}(\mathbf{r}, t) = \sum_n \mathbf{P}(\omega_n) e^{-i\omega_n t} \quad (3.44)$$

and nonlinear polarization is a representation of dielectric polarization with frequency dependence.

The expectation of dipole moment per atom is directly related with nonlinear polarization and that is described as $\widetilde{\mathbf{P}}^{(3)}(\mathbf{r}, t) = N \left\langle p^{(3)} \right\rangle$ for third order susceptibility. Therefore, the polarization for third order susceptibility is represented with using Equation 3.44,

$$P_k(\omega_p + \omega_q + \omega_r) = \sum_{hij} \sum_{pqr} \chi^{(3)}_{kjih}(\omega_\sigma, \omega_r, \omega_q, \omega_p) E_j(\omega_r) E_i(\omega_q) E_h(\omega_p) \quad (3.45)$$

where ω_p, ω_q and ω_r are input laser and output emission frequencies and ω_σ summation of the frequencies ($\omega_\sigma = \omega_p + \omega_q + \omega_r$).

The result of third order susceptibility from Equation 3.45 is written as,

$$\begin{aligned} \chi^{(3)}_{kjih}(\omega_\sigma, \omega_r, \omega_q, \omega_p) &= \frac{N}{\hbar^3} \wp_I \sum_{mnv} \frac{\mu^k_{gv} \mu^j_{vn} \mu^i_{nm} \mu^h_{mg}}{\left(\omega_{vg} - \omega_p - \omega_q - \omega_r\right) \left(\omega_{ng} - \omega_p - \omega_q\right) \left(\omega_{mg} - \omega_p\right)} \\ &+ \quad 47 \text{ other terms} \end{aligned} \quad (3.46)$$

where $\wp_I$ is the intrinsic operator that represents permutation of ω_r,ω_q and ω_p of the applied field. Each one of 48 terms from third order susceptibility may creates different nonlinear processes. The popular processes using third order susceptibility are frequency conversion, third-harmonic generation and four-wave-mixing (FWM) process. The basic properties of FWM process will be discussed in 'Four Wave Mixing' part of the chapter.

3.4.2. Third Order Nonlinear Effects

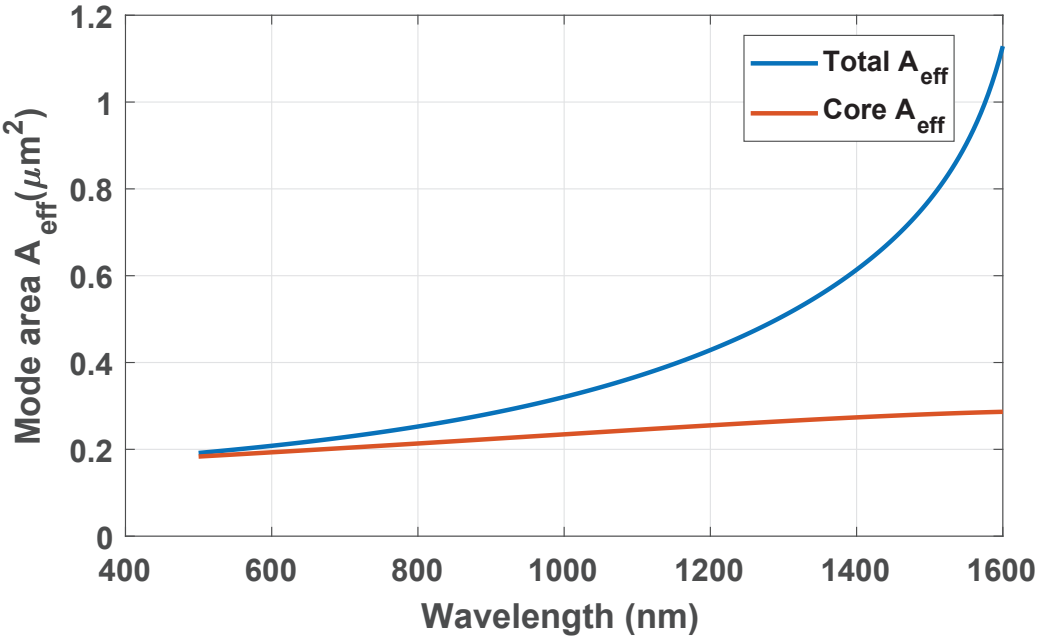

Figure 3.7. Total and core mode area depend on wavelength for Si_3N_4 waveguide

The distribution of electric field is change with wavelength and size of core. We define the size of Si_3N_4 core of waveguide as 650×600 nm^2. We can calculate effective mode of area with surface integral of electric field;

$$A_{eff} = \frac{\left(\int\int_{-\infty}^{+\infty} |E(x,y)|^2 dxdy\right)^2}{\int\int_{-\infty}^{+\infty} |E(x,y)|^4 dxdy}. \tag{3.47}$$

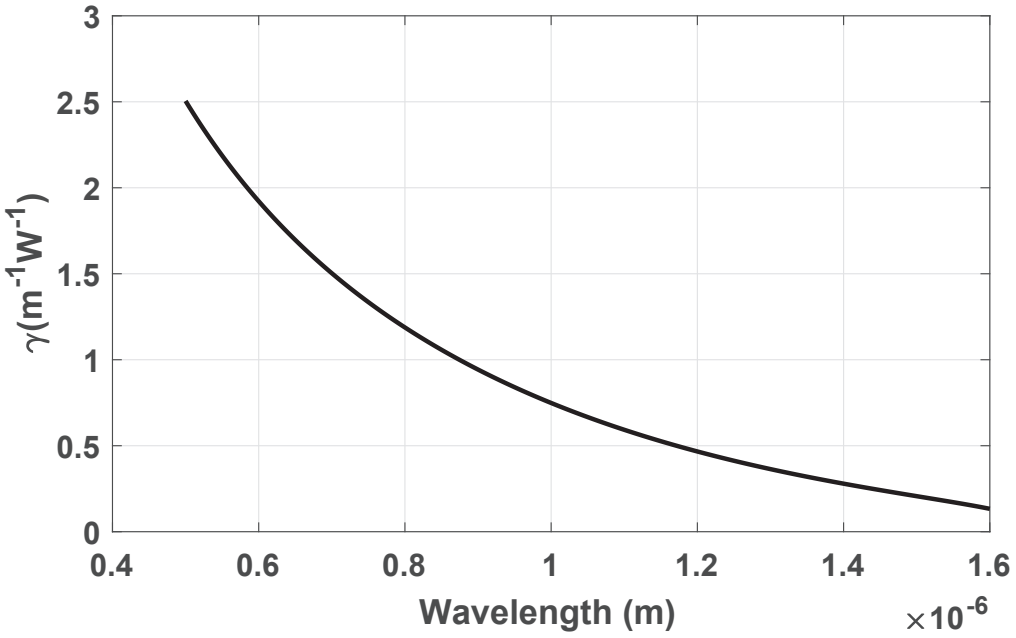

Figure 3.8. The order nonlinear effects changes depend on wavelength

Effective mode area is a parameter shows the properties of confinement to waveguide. Figure 3.7 shows the total and the core confinements with integration on total area and core of waveguide for TE_{00} mode. The core effective mode area increase linearly but A_{eff} is not increase linearly depend on the wavelength. The difference between the total and core effective mode area can define as loss of confinement. For this core size, the loss is recoverable to 800 nm and not grater than 20%. Moreover, the effective mode area is a important parameter for third order nonlinear effects.

The nonlinear susceptibility gives an intensity dependence of the refractive index is expressed as;

$$n(\omega, I) = n_0(\omega) + n_2 \cdot I \tag{3.48}$$

where I is intensity of electric field, n_0 is weak field refractive index and n_2 is the nonlinear refractive index and known as Kerr index. The relation between the Kerr index and third order susceptibility is written as;

$$n_2 = \frac{3}{4n_0\epsilon_0 c} \cdot \chi^{(3)}. \tag{3.49}$$

The Kerr index n_2 is reported as $2.4{\cdot}10^{-19}$ m^2W^{-1} in Ikeda et al. (2008) for Si_3N_4

waveguide. The Kerr index is a parameter of third order nonlinear effects with effective mode area (Boyd, 2000);

$$\gamma = \frac{n_2 \cdot \omega}{A_{eff} \cdot c} \tag{3.50}$$

Figure 3.8 is the graphical description of Equation 3.50 for Si_3N_4 waveguide. In the long wavelength, the third order nonlinear effects on waveguide is decreasing. The calculation shows that nonlinear effects has accessible values for photon pair generation at 780 nm. The photon pair generation from this specific geometry will be discussed in the next section.

3.5. Photon Pair Generation

In generation of photon pairs, nonlinear crystals such as periodically-poled KTP or $LiNbO_3$ are used with parametric down-conversion (PDC) process. This nonlinear crystals have second order susceptibility ($\chi^{(2)}$) and are not available for chip scale. Moreover, silicon based nonlinear materials can create a suitable platform for chip scale and have third order susceptibility ($\chi^{(3)}$) with four wave mixing (FWM) process to photon pair generation.

In this section, we will discuss the basic properties of FWM and show the calculations for Si_3N_4 waveguide.

3.5.1. Four Wave Mixing

Four wave mixing is third order nonlinear process that is designated with two pump waves, one signal and an idler waves. Susceptibility of FWM process can be described with adapted version of Equation 3.46, idler wave susceptibility can be written as;

$$\begin{aligned} \chi^{(3)}(\omega_{idler}) &= \frac{N}{\hbar^3}\wp_I \sum_{mnv} \frac{\mu_{gv}\mu_{vn}\mu_{nm}\mu_{mg}}{(\omega_{vg} - 2\omega_p + \omega_s)(\omega_{ng} - 2\omega_p)(\omega_{mg} - \omega_p)} \\ &+ \text{ 3 resonance terms} \end{aligned} \tag{3.51}$$

where ω_p is frequency of pump, ω_s and ω_i represent the frequency of signal and idler. We can write signal wave susceptibility $\chi^{(3)}(\omega_{signal})$ similarly.

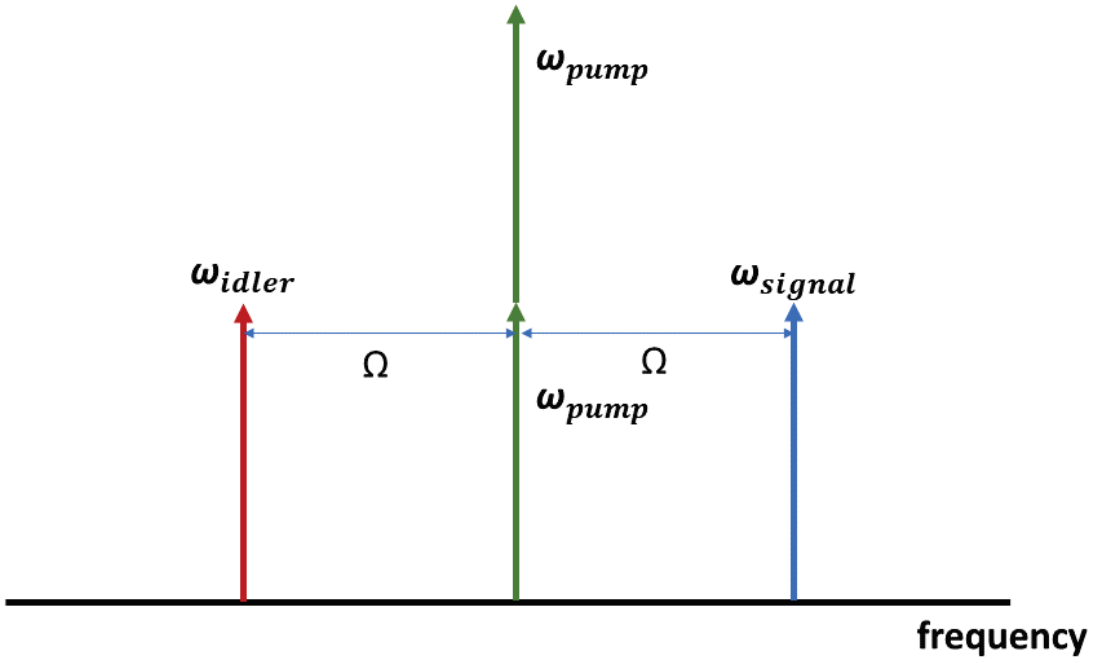

Figure 3.9. Schematically four wave mixing process

Figure 3.9 is a basic schematic representation of FWM process. Ω is frequency difference between pump and signal or idler ($\Omega = \omega_p - \omega_i = \omega_s - \omega_p$). Four wave mixing process must provide energy and momentum conservation. Energy conservation including the pump, signal and idler for degenerate FWM process is written as;

$$2\hbar\omega_p = \hbar\omega_s + \hbar\omega_i, \tag{3.52}$$

where $\hbar$ refer the Planck constant.

The momentum conservation and phase matching requirement give to us same physical background in FWM. The phase matching is described as (Kelley et al., 2001);

$$\begin{aligned} \Delta k &= 2k_p - k_s - k_i = 0, \\ \Delta\beta &= 2\beta_p - \beta_s - \beta_i = 0 \end{aligned} \tag{3.53}$$

where k is wavevector and β is propagation coefficient depending on frequency.

In FWM process idler waves are included annihilated photons and signal waves are created photons from nonlinear medium. This photons must provide physical conservation rules. Moreover, we need to phase mismatching to apply FWM process. The effective mismatch,κ, is written as (Boyd, 2000);

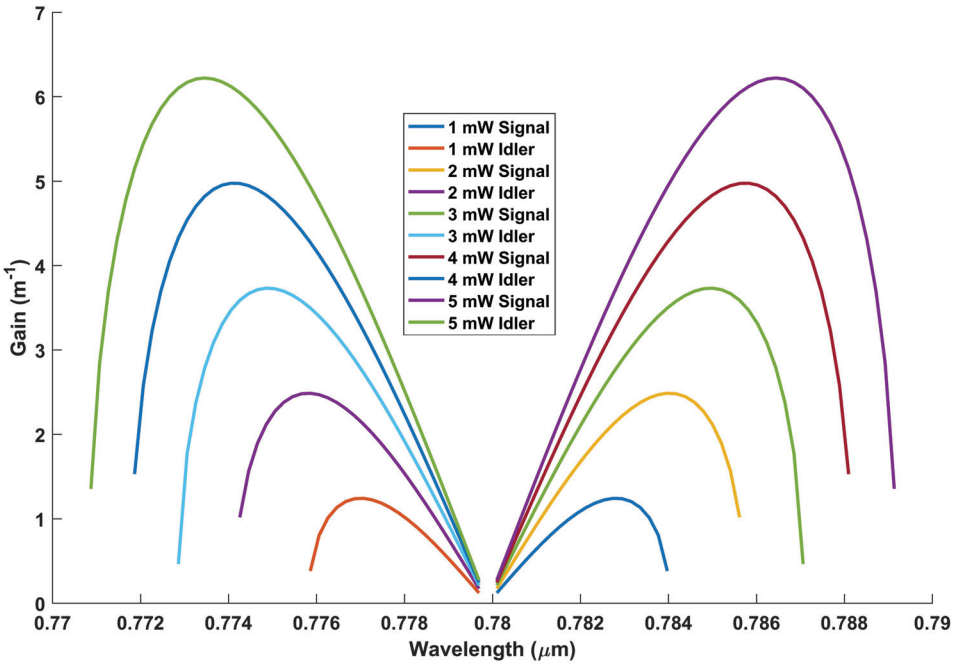

Figure 3.10. Variation of parametric gain for idler and signal waves

$$\kappa = 2\beta_p - \beta_s - \beta_i + 2\gamma P \tag{3.54}$$

where P is power of each pump. γP is nonlinear phase shift that is calculated from Kerr effect. The Equation 3.54 can be applied for photon pair generation, when all waves travel in the same mode and dispersion of the waveguide is bigger than zero but also near the zero.

The parametric gain of FWM is written as;

$$g = \sqrt{(\gamma P)^2 - (\kappa/2)^2} \tag{3.55}$$

where g is parametric gain as a function of effective mismatch, κ. The maximum gain occurs at $\kappa = 0$, and equal to γP with $\Delta\beta = -2\gamma P$.

Figure 3.10 shows the parametric gain with idler and signal waves with different pump powers. The gain is calculated for 650×600 nm^2 Si_3N_4 waveguide upto SiO_2 substrate. The effective wavenumber mismatches are evaluated for each wavelength with 780 nm pump. For each wavelength around 780 nm, the gain is calculated with different

powers. Each power of pump creates different gain scale for signal and idler waves. Moreover, each gain scale has different maximum points. Therefore, the power of pump is ensured the control of frequency difference between pump wave and signal or idler wave.

3.6. Conclusion

In this chapter of the thesis we investigate to design of an integrated silicon nitride waveguide for photon pair generation with four wave mixing process. Firstly, we discussed type of waveguides and study about mode calculation of the waveguides and also we explain different polarization direction creates TE and TM modes. Secondly, we introduce the dispersion calculation to decide the geometry of waveguide. In this part the optimal geometry of silicon nitride waveguide on silicon dioxide substrate found 650×600 nm^2 from zero dispersion wavelength calculation. Finally, effective mode area calculation was finish point of the electromagnetic wave calculations.

Four wave mixing is a nonlinear process of third order. Therefore, we investigate the nonlinear properties of susceptibility and we explain nonlinear effects due to silicon nitride waveguide. Moreover, four mixing process is applied silicon nitride waveguide has a specific geometry (650×600 nm^2) and we show gain process of photon pair generation with 780 nm pump wavelength.

In summary we design an integrated 650×600 nm^2 silicon nitride waveguide on silicon dioxide substrate to use photon pair generation using the four wave mixing process at near 780 nm pump wavelength .

CHAPTER 4

CONCLUSION

In this thesis the temperature dependence of ZPL emission from the point defects in hBN and design of integrated Si_3N_4 waveguide have been investigated. Room and low temperature ZPL shapes are showed theoretically and experimentally. We designed a waveguide for photon pair generation at near 780 nm.

In Chapter 2 we worked on optical properties of defects centers on hBN to show the quantum emission from discrete energy states. We found $\sim$0.4 mW saturation power and $\sim$90 visibility from emitter at 563 nm and showed that hBN defect centers have different dipole orientations. Then Raman shift of hBN was founded 169 meV (1369 cm^{-1}) that represented the energy difference between electronic states. The lineshape of ZPL emission is affected from phonons. The phonon vibrations are directly related to temperature of the sample. Therefore, we investigated temperature dependence measurements and showed changes in FWHM as $\sim$2 nm and shifting in center of ZPL as $\sim$1.6 nm at temperatures that are between 330 K and 78 K. Additionally, FWHM at 78 K after the deconvolution method, was found 0.044 nm. The result is the most sharp ZPL from defects centers in multilayer hBN flakes at 78 K in the literature.Future study about defects center in hBN is creation of controllable emission lines from chemical vapor deposition (CVD) hBN defect centers and constitute impurities on CVD hBN.

In chapter 3 we investigated on design of a waveguide to photon pair generation. For 780 nm pump wavelength, we determined a Si_3N_4 waveguide size as 650×600 nm^2 with SiO_2 substrate according to zero dispersion wavelength. We showed photon pairs using degenerate four wave mixing process and investigate on nonlinear effects to calculation the gain of photon pair generation. Future works about photon pair generation is designed a ring resonator cavity for Si_3N_4 waveguide to decrease the efficiency and continue with experimental measurements.

REFERENCES

Agha, I., M. Davanço, B. Thurston, and K. Srinivasan (2012). Low-noise chip-based frequency conversion by four-wave-mixing Bragg scattering in SiN_x waveguides. *Optics Letters 37*(14), 2997.

Bourrellier, R., S. Meuret, A. Tararan, O. Stéphan, M. Kociak, L. H. G. Tizei, and A. Zobelli (2016). Bright uv single photon emission at point defects in h-bn. *Nano Letters 16*(7), 4317–4321.

Boyd, R. W. (2000). *Nonlinear Optics*.

Cassabois, G., P. Valvin, and B. Gil (2016). Hexagonal boron nitride is an indirect bandgap semiconductor. *Nature Photonics* (January).

Cazzanelli, M., F. Bianco, E. Borga, G. Pucker, M. Ghulinyan, E. Degoli, E. Luppi, V. Véniard, S. Ossicini, D. Modotto, S. Wabnitz, R. Pierobon, and L. Pavesi (2011). Second-harmonic generation in silicon waveguides strained by silicon nitride. *Nature Materials 10*(12), 1–7.

Davies, G. (1981). The Jahn-Teller effect and vibronic coupling at deep levels in diamond. *Reports on Progress in Physics 44*(7), 787–830.

Doni, E. and G. P. Parravicini (1969). Energy Bands and Optical Properties of Hexagonal Boron Nitride and Graphite. *Il Nuovo Cimento 64*(1), 117–144.

Dowling, J. P., K. P. Seshadreesan, and S. Member (2015). Quantum optical technologies for metrology , sensing and imaging. *arXiv*, 1–12.

Exarhos, A. L., D. A. Hopper, R. R. Grote, A. Alkauskas, and L. C. Bassett (2017). Optical Signatures of Quantum Emitters in Suspended Hexagonal Boron Nitride. *ACS Nano 11*(3), 3328–3336.

Fox, M. (2001). *Optical Properties of Solids*.

Gordon, L., J. R. Weber, J. B. Varley, A. Janotti, D. D. Awschalom, and C. G. Van de Walle (2013). Quantum computing with defects. *MRS Bulletin 38*(10), 802–807.

Huang, B., H. Xiang, J. Yu, and S. H. Wei (2012). Effective control of the charge and magnetic states of transition-metal atoms on single-layer boron nitride. *Physical Review Letters 108*(20), 1–5.

Ikeda, K., R. E. Saperstein, N. Alic, and Y. Fainman (2008, aug). Thermal and Kerr nonlinear properties of plasma-deposited silicon nitride/ silicon dioxide waveguides. *Optics Express 16*(17), 12987.

Jelezko, F. and J. Wrachtrup (2006). Single defect centres in diamond: A review. *Physica Status Solidi (A) Applications and Materials Science 203*(13), 3207–3225.

Jungwirth, N. R., B. Calderon, Y. Ji, M. G. Spencer, M. E. Flatt??, and G. D. Fuchs (2016, may). Temperature Dependence of Wavelength Selectable Zero-Phonon Emission from Single Defects in Hexagonal Boron Nitride. *Nano Letters 16*(10), 6052–6057.

Kelley, P. L., I. P. Kaminow, and G. G. P. Agrawal (2001). *Nonlinear fiber optics*.

Kianinia, M., B. Regan, S. Abdulkader, T. T. Tran, M. J. Ford, I. Aharonovich, and M. Toth (2017). Robust Solid-State Quantum System Operating at 800 K. *ACS Photonics 4*, 768–773.

Kurtsiefer, C., S. Mayer, P. Zarda, and H. Weinfurter (2000). Stable solid-state source of single photons. *Physical Review Letters 85*(2), 290–293.

Kwiat, P. G., K. Mattle, H. Weinfurter, A. Zeilinger, A. V. Sergienko, and Y. Shih (1995). New high-intensity source of polarization-entangled photon pairs. *Physical Review Letters 75*(24), 4337–4341.

Larach, S. and R. E. Shrader (1956, apr). Electroluminescence from Boron Nitride. *Physical Review 102*(2), 582–582.

Luke, K., Y. Okawachi, M. R. E. Lamont, A. L. Gaeta, and M. Lipson (2015, nov). Broadband mid-infrared frequency comb generation in a Si_3N_4 microresonator. *Optics*

Letters 40(21), 4823.

Malitson, I. H. (1965, oct). Interspecimen Comparison of the Refractive Index of Fused Silica. *Journal of the Optical Society of America 55*(10), 1205.

Michler, P. (2000). A Quantum Dot Single-Photon Turnstile Device. *Science 290*(5500), 2282–2285.

Monroe, C. (2002). Quantum information processing with atoms and photons. *Nature 416*(6877), 238–246.

Ning, T., O. Hyvärinen, H. Pietarinen, T. Kaplas, M. Kauranen, and G. Genty (2013). Third-harmonic UV generation in silicon nitride nanostructures. *Optics Express 21*(2), 4269–4271.

Sanaka, K., K. Kawahara, and T. Kuga (2001). New High-Efficiency Source of Photon Pairs for Engineering Quantum Entanglement. *Physical Review Letters 86*(2), 5620–5623.

Silverstone, J. W., R. Santagati, D. Bonneau, M. J. Strain, M. Sorel, J. L. O'Brien, and M. G. Thompson (2015). Qubit entanglement between ring-resonator photon-pair sources on a silicon chip. *Nature Communications 6*, 7948.

Srivastava, A., M. Sidler, A. V. Allain, D. S. Lembke, A. Kis, and A. Imamoglu (2014). Optically Active Quantum Dots in Monolayer WSe$_2$. *Nature Nanotechnology 10*(6), 491–496.

Steane, A. (1998, feb). Quantum computing. *Reports on Progress in Physics 61*(2), 117–173.

Stoneham, A. M. (2001). *Theory of Defects in Solids:Electronic Structure of Defects in Insulators and Semiconductors*. Oxford University Press.

Takesue, H. (2012). Entangled photon pair generation using silicon wire waveguides. *IEEE Journal on Selected Topics in Quantum Electronics 18*(6), 1722–1732.

Tanzilli, S., W. Tittel, H. D. Riedmatten, H. Zbinden, P. Baldi, and M. D. Micheli (2002).

PPLN waveguide for quantum communication. *PHYSICAL JOURNAL D 160*, 155–160.

Tawfik, S. A., S. Ali, M. Fronzi, M. Kianinia, T. T. Tran, C. Stampfl, I. Aharonovich, M. Toth, and M. J. Ford (2017). First principles investigation of defect emission from hBN. pp. 1–10.

Taylor, R. and C. Coulson (1952). Studies in Graphite and Related Compounds III: Electronic Band Structure in Boron Nitride. *Proceedings of the Physical Society. Section A*.

Thylén, L. and L. Wosinski (2014). Integrated photonics in the 21st century. *Photonics Research 2*(2), 75–81.

Tran, T. T. et al. (2016). Quantum emission from hexagonal boron nitride monolayers. *Nature nanotechnology 11*(1), 37–41.

Vuong, T. Q. P., G. Cassabois, P. Valvin, A. Ouerghi, Y. Chassagneux, C. Voisin, and B. Gil (2016). Phonon-Photon Mapping in a Color Center in Hexagonal Boron Nitride. *Physical Review Letters 117*(9), 1–5.